TOPICAL REVIEW— Magnetism, magnetic materials and interdisciplinary research

Exchange couplings in magnetic films*

Liu Wei(刘 伟)†, Liu Xiong-Hua(刘雄华), Cui Wei-Bin(崔伟斌), Gong Wen-Jie(龚文杰), and Zhang Zhi-Dong(张志东)‡

Shenyang National Laboratory for Materials Science and International Centre for Materials Physics, Institute of Metal Research, Chinese Academy of Sciences, Shenyang 110016, *China*

(Received 24 December 2012)

Recent advances in the study of exchange couplings in magnetic films are introduced. To provide a comprehensive understanding of exchange coupling, we have designed different bilayers, trilayers and multilayers, such as anisotropic hard-/soft-magnetic multilayer films, ferromagnetic/antiferromagnetic/ferromagnetic trilayers, [Pt/Co]/NiFe/NiO heterostructures, Co/NiO and Co/NiO/Fe trilayers on an anodic aluminum oxide (AAO) template. The exchange-coupling interaction between soft- and hard-magnetic phases, interlayer and interfacial exchange couplings and magnetic and magnetotransport properties in these magnetic films have been investigated in detail by adjusting the magnetic anisotropy of ferromagnetic layers and by changing the thickness of the spacer layer, ferromagnetic layer, and antiferromagnetic layer. Some particular physical phenomena have been observed and explained.

Keywords: exchange interaction, magnetic anisotropy, magnetic properties of interfaces (multilayers, superlattices, heterostructures)

PACS: 71.70.Gm, 75.30.Gw, 75.70.Cn **DOI:** 10.1088/1674-1056/22/2/027104

1. Introduction

Exchange couplings in magnetic thin films have attracted much attention in the application areas of permanent magnets, magnetic recording, sensors and spin electronics. So it is interesting to understand the exchange couplings in different magnetic film systems, with materials of different structures and physical properties. Exchange-coupled permanent magnets were first experimentally realized in ribbons by melt-spinning in 1988.[1] The merits of such magnets would be a high saturation magnetization provided by a soft-magnetic phase and an intermediate coercivity provided by a hard-magnetic phase if the two phases are exchange-coupled well. Subsequently, according to one-dimensional (1D) or three-dimensional (3D) theoretical calculations,[2,3] a higher maximum energy product $(BH)_{max}$ would be possible if the particle size (or layer thickness) of the soft-magnetic phase does not exceed the domain thickness of the hard-magnetic phase. However, it is not easy to control the microstructure to realize the good exchange coupling in bulk materials, compared with thin films. So, much work has been done on multilayer or nanostructured films with Nd–Fe–B, Pt–Fe, Sm–Fe or Sm–Co as the hard-magnetic phase.[4–10] It was found that the higher energy product may be obtained in anisotropic exchange-coupled multilayer magnetic films. The exchange coupled NdFeB/spacer layer (Mo)/Fe multilayer with soft-magnetic phase and textured hard-magnetic phase was prepared.[11] If there is no spacer layer and if the ferromagnetic (FM) layers are soft-magnetic and hard-magnetic layers respectively, such FM/spacer layer/FM trilayers prepared in Ref. [11] would turn into the exchange-coupled nanocomposite magnetic films studied previously.[10] If the magnetocrystalline anisotropy of FM layers is small, this trilayer is same structure as Fe/Cr/Fe trilayers[12] with giant magnetoresistance (GMR) effect. If the spacer layer is antiferromagnetic (AFM), sandwiched by Fe or Co ferromagnetic layers, such a trilayer would turn out to be an FM/AFM/FM system with interlayer and interfacial exchange couplings. From the above discussion, we may inspect the exchange couplings in different magnetic film systems from a comprehensive view.

After the first observation of the AFM coupling in Fe/Cr/Fe trilayers,[12] the interlayer coupling has been widely investigated in FM/non-magnetic(NM)/FM systems. Moreover, the GMR effect was found in $[Fe/Cr]_n$ multilayers,[13] which led to the rapid development of spintronics and small high-density hard disks were realized by applying this technology. The GMR effect was first found in an NM medium adjacent to two magnetic layers with AFM coupling. Multilayer GMR effect should at least meet the following three conditions: (i) the transition of two magnetic layers exchange coupling is from FM to AFM; (ii) the diffraction of conduction electrons is dependent on spin direction; the larger the spin-asymmetries, the stronger the GMR effect; (iii) the mean free path that the spin diffusion does not flip should be at least

*Project supported by the National Basic Research Program of China (Grant No. 2010CB934603), Ministry of Science and Technology of China and the National Natural Science Foundation of China (Grant Nos. 50931006, 50971123, and 51271177).

†Corresponding author. E-mail: wliu@imr.ac.cn

‡Corresponding author. E-mail: zdzhang@imr.ac.cn

© 2013 Chinese Physical Society and IOP Publishing Ltd

greater than the superlattice period. The so-called spin valve is induced by the variation of adjacent magnetic ordering but not the NM medium, which also can obtain GMR effect. There are two ways to achieve the spin valve effect: i) two soft-magnetic layers (with small coercivity) are separated by an NM layer, one layer is pinned by an AFM layer due to the exchange-bias effect; ii) two magnetic layers are separated by an NM layer with different coercivity, therefore, only one magnetic layer is reversed by an applied magnetic field, thus the transition from FM to AFM coupling will be obtained, which results in the GMR effect. The advantage of the spin valve structure is that a very low external magnetic field can drive the magnetic layer into a different magnetic ordering, which is very important in high sensitivity device applications.

In this review, at first, we introduce our recent research including magnetic anisotropic behavior, exchange coupling and coercivity mechanism in textured $Nd_2Fe_{14}B/\alpha$-Fe multilayer films and then study the competition between interlayer and interfacial exchange couplings, effects of the magnetocrystalline anisotropy of FM on the exchange coupling in FM/AFM/FM systems. Finally, we turn to interfacial exchange coupling in FM/FM/AFM heterostructures with in-plane and out-of-plane easy axes and exchange coupling and magnetotransport properties in FM/AFM and FM/AFM/FM antidot arrays.

2. Exchange-coupling between anisotropic nanocomposite soft-/hard-magnetic layers

In this part, the preparation, microstructure and magnetic properties will be presented along with exchange coupling of the anisotropic nanocomposite soft-/hard-magnetic layers. $Nd_{16}Fe_{71}B_{13}$ and $Pr_{16}Fe_{71}B_{13}$ was chosen to be the hard-magnetic layer. α-Fe was the soft-magnetic phase. In order to prevent the interdiffusion/alloying and modify the interface between the hard- and soft-magnetic phase, Mo, Cr and Cu were chosen to be the spacer layer. Deposition condition can be referred to Refs. [11], [14]– [16]

2.1. The anisotropic behavior of textured nanocomposite multilayer films

Generally, an easy way to obtain the Nd–Fe–B/α-Fe multilayer film is to deposit α-Fe onto the top of an Nd–Fe–B layer. An Mo (50 nm)/$Nd_{16}Fe_{71}B_{13}$ (800 nm)/Fe (11 nm)/$Nd_{16}Fe_{71}B_{13}$ (800 nm)/Mo (50 nm) trilayer film was fabricated on a heated Si substrate. The X-ray diffraction (XRD) patterns of all textured films show that the (105) reflection has the highest intensity. Figure 1(a) shows the hysteresis loop of the trilayer film at 295 K.[11] The magnetization along the perpendicular direction starts to drop drastically in a positive external field. The results obtained perpendicular and parallel to the film plane are anisotropic. However, exchange-decoupling behavior appears clearly in the perpendicular direction. This indicates that, due to interdiffusion between soft- and hard-magnetic phases in the interface region, the width of the soft-magnetic region is larger than the critical correlation length L_{ex} so that the soft phase is not exchange-coupled with the hard phase.

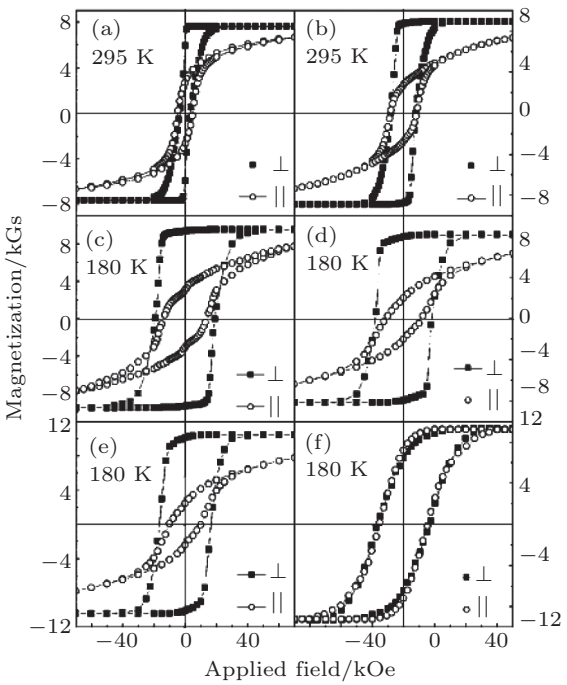


Fig. 1. Hysteresis loops of (a) the trilayer film Mo (50 nm)/$Nd_{16}Fe_{71}B_{13}$ (800 nm)/Fe (11 nm)/$Nd_{16}Fe_{71}B_{13}$ (800 nm)/Mo (50nm) at 295 K, the textured multilayer film Mo (50 nm)/$Nd_{16}Fe_{71}B_{13}$ (800 nm)/Mo (2 nm)/Fe (11 nm)/Mo (2 nm)/$Nd_{16}Fe_{71}B_{13}$ (800 nm)/Mo (50 nm) (b) at 295 K and (c) at 180 K, (d) the textured multilayer film Mo (50 nm)/$Nd_{16}Fe_{71}B_{13}$ (800 nm)/Mo (4 nm)/$Nd_{16}Fe_{71}B_{13}$ (800 nm)/Mo (50 nm) at 180 K, (e) the textured single-layered film Mo (50 nm)/$Nd_{16}Fe_{71}B_{13}$ (800 nm)/Mo (50 nm) at 180 K, (f) the isotropic multilayer film Mo (50 nm)/$Nd_{16}Fe_{71}B_{13}$ (800 nm)/Mo (2 nm)/Fe (11 nm)/Mo (2 nm)/$Nd_{16}Fe_{71}B_{13}$ (800 nm)/Mo (50 nm) at 180 K, with the magnetic field applied parallel (∥) and perpendicular (⊥) to the film plane,[11] 1 Gs=10^{-4} T.

In order to prevent the interfacial diffusion, an Mo (2 nm) was deposited between Fe layer and Nd–Fe–B layer. An Mo (50 nm)/Nd–Fe–B (800 nm)/Mo (2 nm)/Fe (11 nm)/Mo (2 nm)/Nd–Fe–B (800 nm)/Mo (50 nm) multilayer film was prepared. The hysteresis loops measured at 295 K are shown in Fig. 1(b). Smooth loops can be observed along perpendicular and parallel directions. It can be seen that coercivity is increased from 4 kOe (1 Oe = 79.5775 A/m) in Fig. 1(a) to 10 kOe with better squareness, indicating the good exchange-coupling between soft/hard magnetic phases. Such a sandwiched microstructure can be proved by bright field and high-resolution transmission electron microscopy (HRTEM) images, as shown in Fig. 2. From Fig. 2(a), the columnar 2:14:1 grains are very clear. The Mo/Fe/Mo stack layer appears in between two Nd–Fe–B layers. In the HRTEM image, a bright line between the Nd–Fe–B layer and the Fe layer corresponds

to the Mo spacer layer. That indicates that the soft/hard magnetic phases are well separated by the Mo spacer layer and interfacial diffusion is prevented. This means that by using the spacer layer, exchange-coupled hard/soft magnetic multilayer film with textured microstructure can be fabricated.

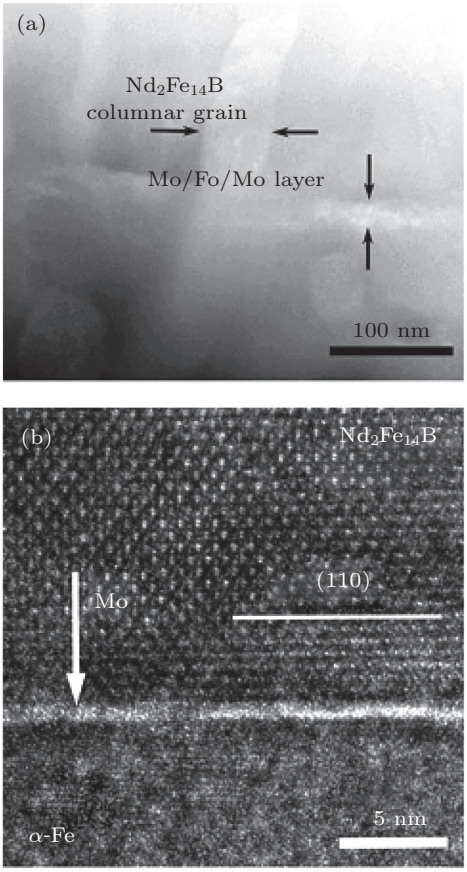


Fig. 2. Cross-sectional morphology image (a) and HRTEM image (b) at the interface region of the anisotropic nanocomposite multilayer film Mo (50 nm)/$Nd_{16}Fe_{71}B_{13}$ (800 nm)/Mo (2 nm)/Fe (11 nm)/Mo (2 nm)/$Nd_{16}Fe_{71}B_{13}$ (800 nm)/Mo (50 nm).[11]

The hysteresis loops at 180 K of the anisotropic nanocomposite Mo (50 nm)/$Nd_{16}Fe_{71}B_{13}$ (800 nm)/Mo (2 nm)/Fe (11 nm)/Mo (2 nm)/$Nd_{16}Fe_{71}B_{13}$ (800 nm)/Mo (50 nm) multilayer film are shown in Fig. 1(c). A good squareness of the demagnetization curve is observed in the direction perpendicular to the film plane. At 180 K, a clear kink in the hysteresis loop is found in the direction parallel to the film plane, which indicates exchange-decoupling between hard and soft phases in the film. It is surprising that different exchange-coupling behavior is observed in the two measuring directions.

The thickness of the α-Fe layer was changed to investigate its effect on the exchange-coupling between the soft/hard phases. Due to the existence of the Mo spacer layer, an effective critical correlation length L_{ex}^{eff} is proposed which is represented by the critical thickness of α-Fe at which a kink occurs in the demagnetization curve with increasing thickness of α-Fe. The effective critical correlation lengths at 295 K and 180 K in the two measuring directions are listed in Table 1. It is found that the effective critical correlation length is always smaller at 180 K than at 295 K, both perpendicular and parallel to the film plane. This temperature dependence is consistent with what is found in the isotropic case and is due to the enhanced magnetocrystalline anisotropy at lower temperature. However, in the textured films, in contrast to the isotropic films, L_{ex}^{eff} is anisotropic and always larger in the perpendicular direction than in the parallel direction, both at 295 K and at 180 K. In order to confirm that the constricted shoulders originate from the exchange-decoupling between soft and hard phase due to the existence of the α-Fe layer, we prepared a textured trilayer film Mo (50 nm)/$Nd_{16}Fe_{71}B_{13}$ (800 nm)/Mo (4 nm)/$Nd_{16}Fe_{71}B_{13}$ (800 nm)/Mo (50 nm), in which the soft α-Fe layer is decreased to zero and a textured single-layered film Mo (50 nm)/$Nd_{16}Fe_{71}B_{13}$ (800 nm)/Mo (50 nm) and measured their hysteresis loops at 180 K both parallel and perpendicular to the film plane. (See Figs. 1(d) and 1(e)). It is clear that the demagnetization is smooth and that, in both directions, there are no kinks in the loop, confirming that the constricted shoulders are related with the α-Fe layer and indeed caused by exchange-decoupling between the soft and hard phases parallel to the film plane. Moreover, it is shown that there are no kinks as long as the thickness of the soft layer is below a critical value (See Table 1), which also proves that the exchange-decoupling is strongly related to the soft phase.

Table 1. The effective critical correlation length L_{ex}^{eff} for textured $Nd_2Fe_{14}B/\alpha$-Fe multilayer films in two directions at 295 K and 180 K.[11]

	295 K	180 K
L_{ex}^{eff} (perpendicular direction ($\perp$))	38 nm	26 nm
L_{ex}^{eff} (parallel direction ($\parallel$))	18 nm	10 nm

In comparison with the microstructure of the isotropic film, it is clear that the only difference is that the hard phase is of textured growth. Good squareness of hysteresis loops in the direction perpendicular to the film (the c axis of the columnar grains) means that $N_\perp$ is close to 0 and $N_\parallel$, perpendicular to the c axis of the columnar grains (in-plane direction of the film), is much larger than $N_\perp$. This is opposite to the case of isotropic multilayer films where $N_\perp$ is larger than $N_\parallel$. Therefore, it is easy to understand that additional shape anisotropy besides the magnetocrystalline anisotropy should be overcome when the demagnetization process is in the direction perpendicular to the c axis of columnar grains (in-plane direction of the film) compared with the demagnetization along the c axis of columnar grains (perpendicular to the film). To account for the shape anisotropy, a total effective anisotropy parallel to the film, $\langle K_{eff}\rangle = \langle K_{mag}\rangle + \langle K_{shape}\rangle$, is proposed where $\langle K_{mag}\rangle$ and $\langle K_{shape}\rangle$ represent the magnetocrystalline anisotropy and the shape anisotropy, respectively. Taking the shape anisotropy into consideration, we propose, $L_{ex} = \pi\ (A/\langle K_{eff}\rangle)^{1/2}$, in accordance with Ref. [2].

When the effective critical correlation length L_{ex}^{eff} is measured in the parallel direction it will be $\pi(A/(\langle K_{mag}\rangle + \langle K_{shape}\rangle))^{1/2}$, which is smaller than its value $\pi(A/K_{mag})^{1/2}$ in the perpendicular direction, both at low temperature and at room temperatures, as observed experimentally. Moreover, $\langle K_{mag}\rangle$ is larger at 180 K than at room temperature, which leads to a smaller L_{ex}^{eff} at 180 K than at room temperature for both directions, just like in the case of isotropic films. In order to prove what we proposed above, we have measured the hysteresis loops at 180 K of an isotropic multilayer film Mo (50 nm)/$Nd_{16}Fe_{71}B_{13}$ (800 nm)/Mo (2 nm)/Fe (11 nm)/Mo (2 nm)/$Nd_{16}Fe_{71}B_{13}$ (800 nm)/Mo (50 nm) (Fig. 1(f)). Because the grains of the hard phase are isotropic in the film, the film shape gives rise to a slight difference between the two measuring directions. However, no kinks are observed in either direction, showing that the anisotropic correlation length found in the textured exchange-coupled hard/soft films is really due to the shape anisotropy of the textured structure of the hard phase.

2.2. Coercivity mechanism

Since the Nd–Fe–B/α-Fe anisotropic nanocomposite multilayer films with columnar grain shape can be fabricated, it is interesting to clarify the coercivity mechanism. The Mo (50 nm)/$Nd_{16}Fe_{71}B_{13}$ (800 nm)/Mo (x nm)/Fe (11 nm)/Mo (x nm)/$Nd_{16}Fe_{71}B_{13}$ (800 nm)/Mo (50 nm) films ($x = 2$ nm, 4 nm, 6 nm) with different thicknesses of Mo spacer layer were prepared.[15] The temperature dependence of the coercivity of these anisotropic nanocomposite films measured along perpendicular direction is shown in Fig. 3. It is obvious that with decreasing measuring temperature from 295 K to 150 K the coercivity is enhanced due to stronger magnetocrystalline anisotropy.

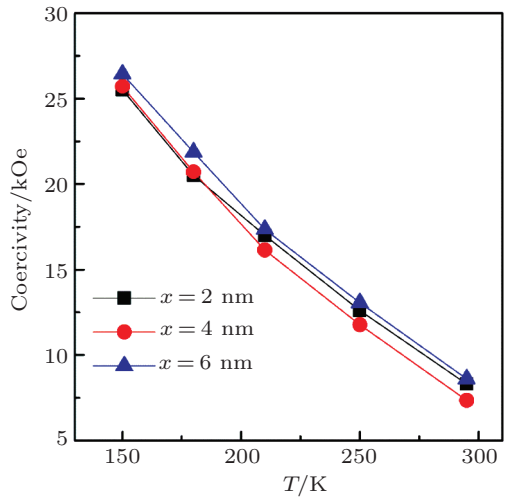


Fig. 3. The coercivity temperature dependence of the multilayer film Mo (50 nm)/$Nd_{16}Fe_{71}B_{13}$ (800 nm)/Mo (x nm)/Fe (11 nm)/Mo (x nm)/$Nd_{16}Fe_{71}B_{13}$ (800 nm)/Mo (50 nm) films ($x = 2$ nm, 4 nm, 6 nm).[15]

In order to find out the coercivity mechanism, the Krönmuller model,[17] ${}_iH_c = \alpha H_N - N_{eff} M_S$, is applied for the multilayer films. Here, ${}_iH_c$, H_N, and M_S are the coercivity, nucleation field, and saturation magnetization. α and N_{eff} are the micromagnetic parameters. Coercivity ${}_iH_c$ and saturation magnetization M_S can be obtained from hysteresis loops measured at different temperatures. α can be expressed by $\alpha_K \alpha_\Phi \alpha_{ex}$, where α_Φ describes the misalignment of moments in the hard magnetic phase and α_{ex} is the parameter considering the exchange-coupling effect. In the $Nd_2Fe_{14}B$ system, the determination of nucleation field is a little difficult because the first-order magnetocrystalline constant K_1 first increases and then decreases with decreasing temperature. So, H_N can be expressed in different terms in a divided temperature region[18]

$$H_N^1 = \frac{2K_1}{M_s}, \quad K_1 > 4K_2, \quad T > 250\ \text{K}, \tag{1}$$

$$H_N^2 = \frac{8K_2}{M_S}\left[\frac{K_1 + 2K_2}{6K_2}\right]^{3/2}, \quad -2K_2 < K_1 < 4K_2, \quad T \le 250\ \text{K}. \tag{2}$$

Considering the exchange-coupling between soft/hard-magnetic phase, one should consider the exchange interaction coefficient, denoted as $\alpha_{ex} = (1 + 6\beta L_{ex}/d)^{-1}$.[19] Hence the Krönmuller equation would be represented as

$$H_c = \frac{\alpha_K \alpha_\Phi^{min}}{1 + 6RL_{ex}/d} H_N - \frac{N_{eff}}{1 + 6RL_{ex}/d} M_S, \tag{3}$$

where L_{ex} is the critical ferromagnetic exchange length, d is the grain size, α_Φ^{min} is the minimum value of α_Φ.

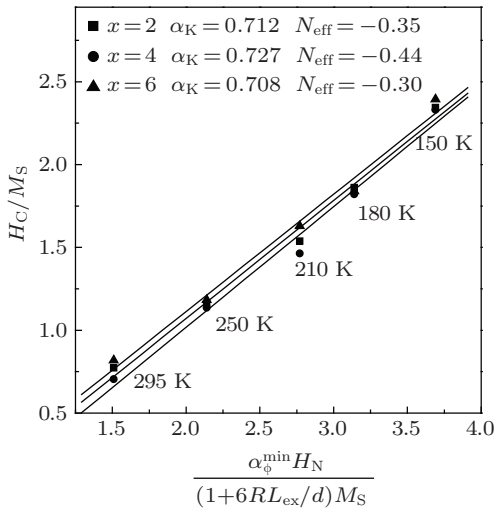


Fig. 4. Dependence of H_C/M_S with $\alpha_\phi^{min} H_N/(1+6RL_{ex}/d)M_S$ for Mo (50 nm)/$Nd_{16}Fe_{71}B_{13}$ (800 nm)/Mo (x nm)/Fe (11 nm)/Mo (x nm)/$Nd_{16}Fe_{71}B_{13}$ (800 nm)/Mo (50 nm) films ($x = 2$ nm, 4 nm, 6 nm). (Inset shows fitted parameters α_K and N_{eff} for each film.)[15]

Figure 4 shows the fitted plots of H_c/M_S versus $\alpha_\Phi^{min} H_N/(1+6RL_{ex}/d)M_S$ for Mo (50 nm)/$Nd_{16}Fe_{71}B_{13}$ (800 nm)/Mo (x nm)/Fe (11 nm)/Mo (x nm)/$Nd_{16}Fe_{71}B_{13}$ (800 nm)/Mo (50 nm) films ($x = 2$ nm, 4 nm, 6 nm). It is evident that a nearly perfect linear relationship exists over the whole temperature region. Fitting parameters α_K and N_{eff} are

obtained and shown in the inset of Fig. 4. It can be seen that α_K values for films with Mo layer thickness of $x = 2$ nm, 4 nm, and 6 nm are mainly concentrated at $\alpha_K \approx 0.7$, suggesting that a uniform coercivity mechanism is predominant in this series. α_K describes the influence of microstructure defects on the nucleation field. Large α_K means a weak influence of inhomogeneous microstructure and fewer nucleation centers and crystalline defects. Referring to the micromagnetic model,[20] $\alpha_K > 0.3$ is considered to be compatible with the reversal-domain nucleation mechanism. Therefore, it is concluded that the nucleation mechanism of reversal domains is dominant in the first three films.

2.3. Exchange-coupling with spacer layer

From the above experiments, it is worth noticing that even if there are several nanometers of spacer layers, the exchange-coupling between the soft-magnetic and the hard-magnetic phases can still happen. As mentioned above, once there are spacer layers between the soft/hard magnetic layers, the structure is like FM/NM/FM[21] trilayer or FM/NM/AFM[22] exchange-bias systems. In the latter two cases, the NM spacer layer plays an important role in mediating the interlayer exchange coupling.

The strength of the exchange-coupling between soft/hard-magnetic layers is related to L_{ex}^{eff}. Due to the film structure's similarity with that of FM/NM/FM[21] trilayer or FM/NM/AFM[22] exchange-bias systems, it is interesting to investigate how the spacer layer affects the exchange coupling in hard-magnetic-layer/spacer-layer/soft-magnetic-layer systems. So, in the following part, some factors that influence the exchange-coupling are discussed.[16]

As can be seen in Fig. 1, it is clear that L_{ex}^{eff} shows an anisotropic behavior in textured multilayer films. By gradually increasing the thickness of the Fe layer, the L_{ex}^{eff} along directions perpendicular or parallel to the thin film plane measured at 295 K or 180 K can be obtained for a certain thickness of spacer layer. The inset figure in Fig. 5 shows an XRD pattern which is typical of all multilayer films with spacer layers. It can be seen that the intensity of the (105) reflection is greatly enhanced, indicating the structure of strong c-axis textured films. In Fig. 5, the dependence of L_{ex}^{eff} on the thickness of the Mo spacer layer is shown, which was measured at 180 K and 295 K with the field applied either perpendicular or parallel to the film plane. Because L_{ex}^{eff} (180 K, $\|$) is very small and rapidly decreases to zero, its dependence on the thickness of Mo spacer layer is not obvious and is shown in Fig. 5. L_{ex}^{eff} (295 K, $\perp$), which means L_{ex}^{eff} measured at 295 K along the direction perpendicular to the thin film plane decreases with increasing thickness of the Mo spacer layer, but it does not vary significantly when the thickness of the Mo spacer layer varies between 4 nm and 6 nm. When the thickness of the spacer layer exceeds 8 nm, the L_{ex}^{eff} (295 K, $\perp$) decreases rapidly to zero. For the same thickness of spacer layer, the value of L_{ex}^{eff} (180 K, $\perp$) becomes smaller in comparison with that at room temperature, due to the enhanced magnetocrystalline anisotropy. In addition, the value of L_{ex}^{eff} (295 K, $\|$) is also smaller than L_{ex}^{eff} (295 K, $\perp$) with spacer layers of the same thickness, due to the contribution of the shape anisotropy of textured hard-magnetic phases. However, the nonlinear dependence of L_{ex}^{eff} (295 K, $\|$) or L_{ex}^{eff} (180 K, $\perp$) on the spacer-layer thickness is similar to that of L_{ex}^{eff} (295 K, $\perp$). Only a vertical shift along the y axis is observed due to the anisotropy.

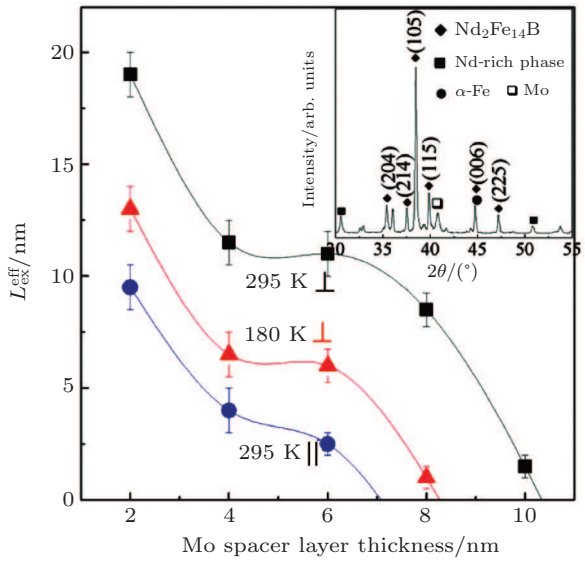


Fig. 5. Dependence of L_{ex}^{eff} on the thickness of the Mo spacer layer in Mo (50 nm)/NdFeB (800 nm)/Mo (x nm)/Fe (y nm)/Mo (x nm)/NdFeB (800 nm)/Mo (50 nm) multilayer films, measured at 180 K and 295 K with the applied field perpendicular and parallel to the film plane. Inset in Fig. 1(a) shows an XRD pattern typical of a textured multilayer film.[16]

In order to identify whether such nonlinear dependence is spacer-layer-dependent, Cu and Cr spacer layers were used. Figure 6 shows the dependence of L_{ex}^{eff} (295 K, $\perp$) on the thickness of spacer layers (Cu or Cr) in NdFeB/α-Fe and Mo in PrFeB/α-Fe multilayers. Those dependencies are qualitatively similar to that of L_{ex}^{eff} (295 K, $\perp$) as shown in Fig. 5, where a flat region can be seen between the thickness of spacer layer from 4 nm to 8 nm, indicating that such nonlinear dependence is not sensitive to the materials chosen for the NM spacer layer or hard-magnetic phases. But at the same thickness of spacer layer, the value of L_{ex}^{eff} is dependent on the spacer layer materials. From Fig. 6, when the spacer layer is thinner than 10 nm, the value of L_{ex}^{eff} for Cu as the spacer layer is larger than the value of L_{ex}^{eff} for Cr as spacer layer, which may be due to the intrinsic properties of spacer materials. When the thickness of the α-Fe layer is extrapolated to zero, this thickness of spacer layer is defined to be the decay length, indicating the depth that the soft-/hard-magnetic exchange coupling can propagate

in the spacer layer. As seen from Fig. 6, for the cases of Cu spacer layer (curve *a*) and Cr spacer layer (curve *b*), the penetration length is around 11 nm. Since the dependence of L_{ex}^{eff} on the thickness of NM spacer layer is plotted along the direction perpendicular to the thin film plane at room temperature, compared with the penetration depth of around 11 nm in thin film with Mo as spacer layer material (dark-square curve of Fig. 5), the penetration depth is not changed for different spacer layer materials. However, penetration depth is a temperature- and texture-direction dependent parameter because it is reduced at lower temperature (triangle red curve in Fig. 5) or along the direction parallel to the thin film (blue circle curve in Fig. 5), due to the enhanced magnetocrystalline anisotropy at low temperature or the contribution of shape anisotropy in the textured structure. When the hard-magnetic layer is changed into a Pr–Fe–B layer with Mo as spacer layer, the penetration length is also around 11 nm (curve *c* of Fig. 6). However, it is worth noting that the exchange-coupling between the soft- and hard-magnetic layers happens even when the thickness of the spacer-layer is as large as 10 nm, much larger than the decay length of 5 nm reported in exchange-biased AF/NM/FM trilayers.[22] Compared with the thickness of the NM spacer layer in FM/NM/FM multilayer films,[21] it is concluded that the exchange coupling between the soft- and hard-magnetic phases is a long-ranged interaction.

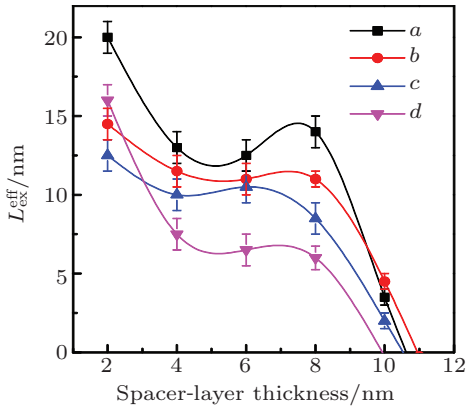


Fig. 6. L_{ex}^{eff} in Mo (50 nm)/*HM* (*z* nm)/*NM* (*x* nm)/Fe (*y* nm)/*NM* (*x* nm)/*HM* (*z* nm)/Mo (50 nm) (*NM* = Mo, Cu or Cr and *HM* = $Nd_{16}Fe_{71}B_{13}$ or $Pr_{16}Fe_{71}B_{13}$) multilayer films at 295 K, with the applied field perpendicular to the film plane. Its dependence on (curve *a*) *NM* = Cu for *HM* = $Nd_{16}Fe_{71}B_{13}$ (800 nm); (curve *b*) *NM* = Cr for *HM* = $Nd_{16}Fe_{71}B_{13}$ (800 nm); (curve *c*) *NM* = Mo for $Pr_{16}Fe_{71}B_{13}$ (800nm), and (curve *d*) Mo for *HM* = $Nd_{16}Fe_{71}B_{13}$ (200nm).[16]

Usually, the Hankel plot[23] is used to clarify the exchange-coupling or the static interaction between neighbor grains in hard magnets or hard/soft composites. The Hankel plot relates the isothermal remanence ratio $m_r(H)$ $(= M_r(H)/M_r(\infty))$, obtained through progressive magnetization, with the demagnetization remanence ratio $m_d(H)$ $(= M_d\ (H)/M_r(\infty))$, obtained through progressive demagnetization from a previously saturated state to the same demagnetization field, where $M_r(\infty)$ is the remanence obtained in the saturated state. It is expressed as $\delta m(H) = m_d(H) - [1 - 2m_r(H)]$.[23] Figure 7 shows the typical Hankel plots of Mo (50 nm)/NdFeB (800 nm)/Cu (6 nm)/Fe (22 nm)/Cu (6 nm)/NdFeB (800 nm)/Mo (50 nm) and Mo (50 nm)/NdFeB (800 nm)/Cr (6 nm)/Fe (21 nm)/Cr (6 nm)/NdFeB (800 nm)/Mo (50 nm) thin film, in which the thickness of α-Fe is the L_{ex}^{eff} for spacer layer of Cu (6 nm) and Cr (6 nm). The coercivities are also marked. Since $\delta m\ (H)$ value is always negative for these two films in Fig. 7. It is proposed that there is at least the existence of magnetostatic interactions between soft- and hard-magnetic layers, which leads to the observed nonlinear dependence.

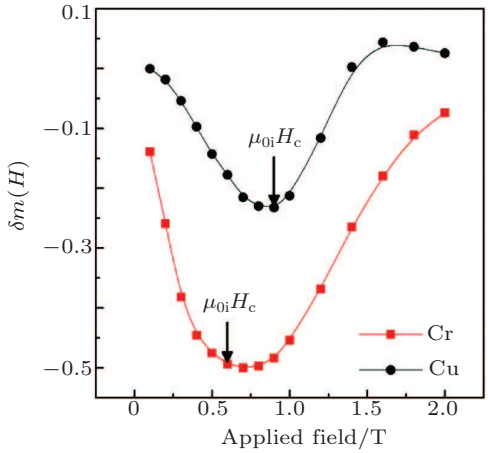


Fig. 7. Variation of $\delta m(H)$ as the function of applied field for the thin film Mo (50 nm)/NdFeB (800 nm)/Cu (6 nm)/Fe (22 nm)/Cu (6 nm)/NdFeB (800 nm)/Mo (50 nm) (dark) and Mo (50 nm)/NdFeB (800 nm)/Cr (6 nm)/Fe (21 nm)/Cr (6 nm)/NdFeB (800 nm)/Mo (50 nm) (red) measured along the direction perpendicular to the film plane.[16]

3. Magnetic exchange coupling in FM/AFM/FM systems

As the discovery of the GMR in Fe/Cr superlattices exhibits broad application prospects, it attracts much attention worldwide. Parkin *et al.* found oscillation of magnetic exchange coupling in FM/NM multilayers in 1990.[24] An obvious GMR effect was observed in Co/Ru, Co/Cr, and Fe/Cr multilayers and the magnetoresistance (MR), saturation field (H_S), or exchange coupling energy (J) oscillated with variation of NM thickness. The GMR and oscillation coupling effects have been found in many multilayers that contain magnetic metal (Fe, Co, Ni) separated by noble metal (Cr, Cu, Ag, Au) or 3d, 4d, 5d NM metal.[21,26–30] Furthermore, the oscillation period of coupling is nearly the same ($P \sim 10$ Å, 1 Å = 0.1 nm) for different NM metals except Cr ($P \sim 18$ Å), which may be due to the special spin density wave (SDW) of Cr's AFM state below the ordering temperature with long wavelength of about 40 Å.[31]

In a thin film multilayer, only a single period was observed at first, then two different oscillation periods were

found in Fe/Cr/Fe (100) trilayer by Unguris *et al.*[31,32] Usually, the short oscillation period is only observed in thin film grown by molecular beam epitaxy (MBE). Theory indicates that the different oscillation period is closely related to Fermi vector length of spacer layer.[33] There are two main factors that affect the coupled oscillation in multilayer films: a) the complex Fermi surface of the intermediate spacer layer — the Fermi vector is a real number for the metal material but is a pure imaginary number for the insulator. This affects the wavelength of the oscillation, the interlayer coupling phase and attenuation range of the coupling strength as the thickness increases; b) the FM spin asymmetric diffraction coefficient in FM/paramagnetic (PM) interface, which is the difference between FM spin-up and spin-down in the interface. It mainly influences the strength of interlayer exchange coupling and the phase of period, in which the second factor is related to the FM material and the thickness of FM.

Early research mainly focused on the first factor, that obvious GMR and oscillation coupling effects were found in the different multilayers, or changed Fermi vector of spacer layer with doping,[34] and they lead to obvious variation of the oscillation period and strength.[35,36] Furthermore, the oscillation of coupling strength with variation of FM thickness was also observed in multilayer systems, which is due to electrons' Bloch vector in the FM layer that occurs like Fabry–Pérot interference as proposed by Bruno.[37] In another way, by changing the diffraction coefficient of the FM layer, i.e. changing the composition of the FM metal, such as Fe–Ni, Co–Ni or Fe–Co–Ni, through changing the different components of FM to vary the diffraction coefficient, thus obvious variation of coupling strength and shift of phase were found in this system.[38–40]

In comparison with FM/NM/FM trilayer, FM/AFM/FM trilayer is more complicated, since it contains additional interfacial exchange coupling between FM/AFM layers. Moreover, usually, the interfacial exchange coupling strength between FM/AFM decreases with increasing temperature, while the variation of interlayer exchange coupling strength between two FM layers with temperature is different for a metallic versus an insulating spacer layer. When a spacer layer is metal, the strength of interlayer exchange coupling decreases with increasing temperature, while for an insulating spacer layer, it increases with increasing temperature. As the variation of interfacial coupling of FM/AFM and interlayer coupling between two FM layers with external conditions in different film systems is very complicated, many physical contents are contained in FM/AFM/FM system.

In 1995, Filipkowski *et al.* reported that in epitaxial CoFe/Mn/CoFe (001) trilayer made by a ferromagnetic resonance method, the coupling angle between two CoFe layers is nearly 90° but not 180° and the coupling energy can be expressed by $F_c = C_+(\phi_1 - \phi_2)^2 + C_-(\phi_1 - \phi_2 - \pi)^2$.[41] Then, in epitaxial Fe_3O_4/NiO/Fe_3O_4 trilayers, the 90° coupling between two FM layers can be observed as NiO thickness changes from 0.7 nm to 5 nm. They attributed this phenomenon to the interface roughness of the AFM spacer layer between the FM layers giving rise to a vertical coupling effect.[42] Previous work on interlayer exchange coupling mainly focused on the same FM layer with AFM spacer layer. Yang *et al.*[43] studied exchange coupling in FM/AFM/FM systems, using different FM materials, FeNi and Co (quite different anisotropy for two FM materials). They found that the coupling angle between two FM layers was different for different FeMn thickness; when $t_{AF} \leq 90$ Å, there was a simple equation: $\theta = 1.76t_{AF}$. As the interfacial coupling in FM/AFM layers, the direction of FeMn's spin moment could mediate magnetic moment direction between Co and FeNi and the AFM ordering took a very important role in the FM/AFM/FM system. Camarero *et al.* also observed vertical interlayer coupling in NiFe/NiO/Co trilayer system and found that when AFM thickness was 25 nm, through numerical simulation, the interface roughness might result in this phenomenon.[44]

Several theoretical models have been proposed to represent the mechanism of interlayer coupling and its oscillation effect, such as the RKKY model,[45,46] free electron model,[47,48] hole binding model,[49] Anderson (or sd mixing) model,[50,51] *ab initio* model,[52,53] and quantum interference model.[54–57] The physical problems are very complex in these models, but no one can explain all the phenomena, such as the origin of its interlayer coupling, strength of coupling, oscillation phase, two oscillation periods with variation of spacer layer thickness and so on. There are mainly three successful models: like-RKKY interaction theory, spin polarization theory of quantum wells and total energy calculations. The RKKY model is proposed to explain the magnetic ordering of metals and alloys exchange coupling between the local magnetic moments. The coupling of the two impurity spins through the medium of the electronic gas and the local magnetic moment's interaction with conduction electrons, together, generate the oscillation strength of the indirect exchange coupling. In multilayer film systems, the interaction of the magnetic moments within the film leads to spin polarization of conducting electrons in the NM spacer layer, which results in magnetic exchange coupling between two FM layers, but it cannot explain the long-period oscillation behavior. Bruno *et al.* considered the film surface atoms' discontinuity and NM metal Fermi surface structure and proposed the relationship between the oscillation period of the magnetic coupling and the Fermi surface of the NM spacer, which theoretically gave two periods consistent with the experimental values.[46] However, as the RKKY theory did not consider the specific structure of the energy band, it could not give oscil-

lation phase and strength of exchange coupling. Total energy calculation based on the NM layer thickness is used to calculate the energy when the exchange interaction between two FM layers is FM or AFM coupling and the strength of exchange coupling can be obtained from the energy difference between the two magnetic states. However, the energy difference is much smaller than the two magnetic ordering energies. Despite the difficulty of achieving convergence of value and the extensive computing time required, theory is usually used to explain the short oscillation period. Recently, based on quantum theory, the quantum interference and quantum well states model was very successful and widely accepted. Beuno's quantum interference theory proposed that the exchange coupling is due to the interference effects of Bloch waves in FM and NM interface diffraction. As the electron state of ultra-thin film is different from that of the block, the direction perpendicular to the film surface is periodically destroyed, corresponding to the discontinuous wave vector and discrete energy $E(k_z)$, which results in magnetic quantum well states. The related wave function is characterized by the fast oscillation Bloch function that is modulated by a slowly varying envelope function. When the multilayer film is replaced by a quantum well potential, the band of wave number that is formed by bound conduction electrons corresponds to the number of layers. With an increase of film thickness, the energy levels of the quantum wells sequentially transect the Fermi surface and with varying spacer thickness $N(E_F)$ oscillates. Quantum interference model explains many phenomena, especially predicts oscillation effect of exchange coupling with the thickness of the ferromagnetic layer and the outer protective layer.

4. Competition between interlayer and interfacial exchange couplings

In FM/AFM/FM systems, only few investigations have focused on the competition between the interfacial coupling between FM and AFM layers and the interlayer coupling between two FM layers. No previous work noted the competition between these two couplings at different temperatures. Based on this fact, we reported experimental observation of this competition at different temperatures T, in Co/AFM/Fe trilayers with the AF insulators Cr_2O_3 and NiO, and the AF metal Cr.[58] The temperature dependence in trilayers with AFM insulating NiO or Cr_2O_3 spacer layer differs from that with AFM metallic Cr. In the insulator case, the enhancement of the interlayer exchange coupling and the reduction of interfacial exchange coupling with increasing temperature results in dominating interlayer exchange coupling at high temperature. In the metallic spacer case, both the couplings decrease with increasing temperature, resulting in decoupling at high temperatures.

The hysteresis loops for Co (3 nm)/NiO (6 nm)/Fe (10 nm) (sample 1) measured at 50 K, 100 K, 150 K and 310 K after ZFC are shown in Fig. 8. All loops are normalized to their saturation magnetization (M_S) and the magnetization corresponding to a step in a loop is called M_P. We define the parameter $L = M_P/M_S$. Clearly, the M–H curves exhibit a small step at 50 K and a linear increase of magnetization at 100 K. A clear step is seen at 150 K but disappears for $T \geq 310$ K. The different values for L at different temperatures are due to the effect of the interfacial and interlayer couplings in trilayers. The tendency observed above in the trilayers with NiO is similar to that with Cr_2O_3 (sample 2).

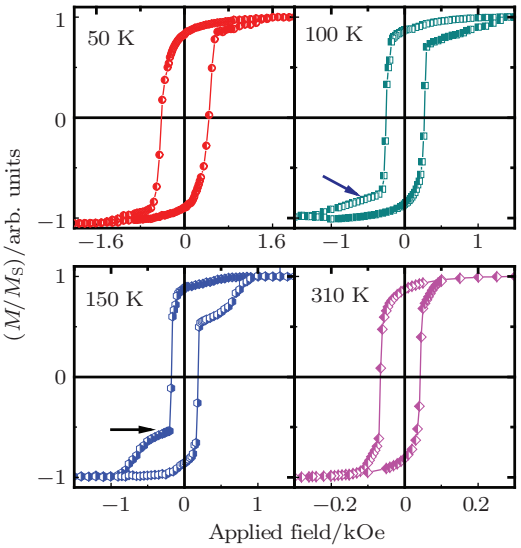


Fig. 8. Hysteresis loops at 50 K, 100 K, 150 K and 310 K of Co (3 nm)/NiO (6 nm)/Fe (10 nm) after ZFC.[58]

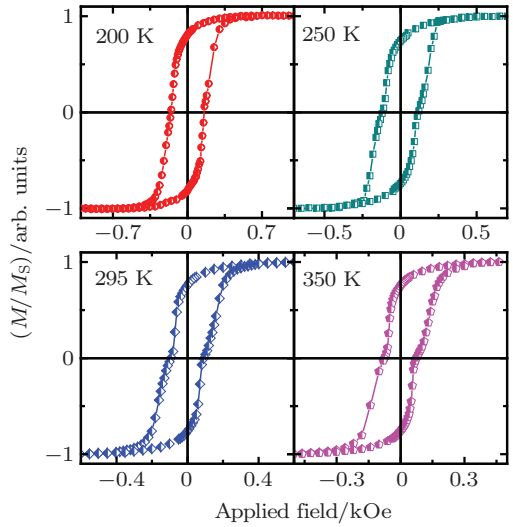


Fig. 9. Hysteresis loops at 200 K, 250 K, 295 K and 350 K of Co (3 nm)/Cr (6 nm)/Fe (10 nm) after ZFC.[58]

For comparison, the hysteresis loops of Co (3 nm)/Cr (6 nm)/Fe (10 nm) (sample 3), recorded at different temperatures after ZFC, are presented in Fig. 9. The FM layers are quite well coupled at $T = 200$ K, whereas the kink observed

at $T \geq 250$ K is indicative of decoupling between two FM layers. The phenomena mentioned above suggest that the variation of the couplings with temperature is quite different for the trilayers with AFM materials of the two different types, i.e., insulator and metal.

In order to study the influence of the FC process on the magnetic properties, the hysteresis loops at 10 K of Co (3 nm)/Cr_2O_3 (6 nm)/Fe (10 nm) (sample 2) after ZFC (black filled circle) and FC (red filled square) in an applied field of 2 kOe are presented in Fig. 10(a). For comparison, the hysteresis loop at 10 K after FC in an applied field of -2 kOe is shown in Fig. 10(b). Figures 10(c) and 10(d) show the major/minor hysteresis loops of sample 2 at 170 K and sample 1 at 200 K, respectively, both after ZFC. It is seen from Fig. 10(a) that the two FM layers switch at the same field in the ZFC loop, but a step is observed in the third quadrant of the FC loop. The value of saturation field H_S of the FC loop about -7 kOe is much larger than that of the ZFC loop, while no step is found in the first quadrant. Both hysteresis loops in Figs. 10(a) and 10(b) reflect the FM interfacial coupling between Fe and Cr_2O_3 and Co and Cr_2O_3 after FC.[59] In Figs. 10(c) and 10(d), the values of minor-loop shift $H_E < 0$ indicate FM interlayer coupling in the trilayers at this temperature.[60]

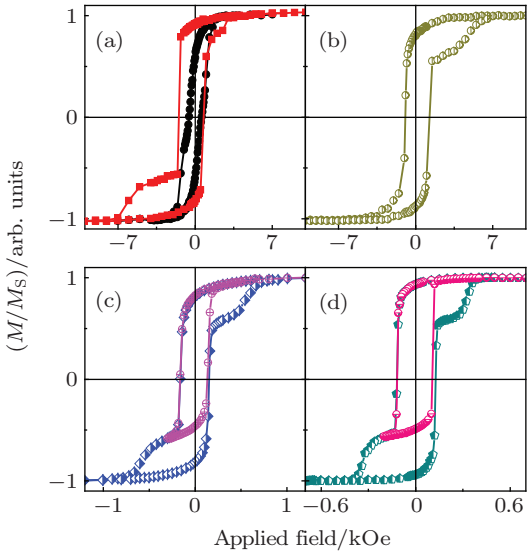


Fig. 10. (a) Hysteresis loops at 10 K of Co (3 nm)/Cr_2O_3 (6 nm)/Fe (10 nm) after ZFC (black filled circles) and FC (red filled squares) in an applied field of 2 kOe. (b) Hysteresis loop at 10 K of Co (3 nm)/Cr_2O_3 (6 nm)/Fe (10 nm) after FC in an applied field of -2 kOe. (c) Major and minor hysteresis loops at 170 K of Co (3 nm)/Cr_2O_3 (6 nm)/Fe (10 nm) after ZFC. (d) Major and minor hysteresis loops at 200 K of Co (3 nm)/NiO (6 nm)/Fe (10 nm) after ZFC.[58]

The temperature dependence of L of samples 1 and 2 after ZFC (the values of L after FC are nearly constant and are not presented here) and M_S of sample 2 after ZFC and FC and sample 1 after ZFC are shown in Fig. 11. It is found that for sample 2, the values of M_S obtained after FC decrease with increasing temperature and they are larger than those after ZFC. The same trend is seen for sample 1 (not shown here). The maxima of M_S after ZFC are found at around 120 K for the trilayers with Cr_2O_3 and at around 150 K for the trilayers with NiO. Thus, the values of M_S at different temperatures after ZFC have been normalized to M_S at 120 K and 150 K for the two samples, respectively (shown in Fig. 11(b)). It is seen in Fig. 11 that the maximum of M_S after ZFC corresponds to the minimum of L (as marked by the dashed arrows), and that the peak temperature of the film with NiO is larger than that of the film with Cr_2O_3. Furthermore, the disappearance of the step is seen at about 220 K and 310 K for the film with Cr_2O_3 and NiO, respectively (see Fig. 11(a)).

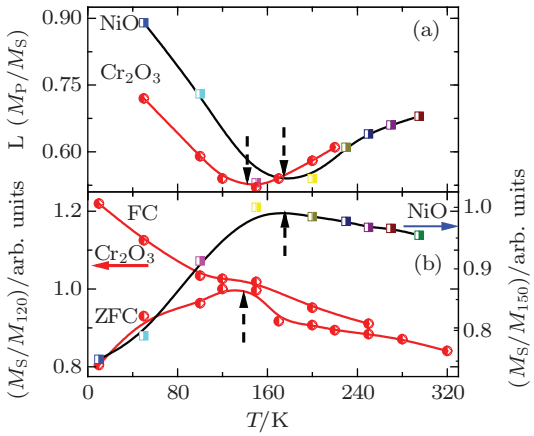


Fig. 11. (a) Temperature dependence of L of Co (3 nm)/NiO (6nm)/Fe (10nm) and Co (3nm)/Cr_2O_3 (6 nm)/Fe (10 nm) after ZFC. (b) Temperature dependence of M_S /M_{120} for Co (3 nm)/Cr_2O_3 (6 nm)/Fe (10 nm) after ZFC and FC and M_S /M_{150} for Co (3 nm)/NiO (6 nm)/Fe (10 nm) after ZFC.[58]

The total free energy E of the Co/AF/Fe trilayers contains four contributions: 1) the interfacial coupling at two interfaces of the AFM layer, 2) the interlayer coupling between the two FM layers, 3) the magnetocrystalline anisotropy of each layer and 4) the Zeeman energy of each layer. The Zeeman energy of each layer and the magnetocrystalline anisotropy of FM layers have little temperature dependence.[61,62] Thus, the main contributions to the energy with temperature come from 1) and 2). $J(T) = J(0)(T/T_0)/\sinh(T/T_0)$,[55,63] where $J(0)$ is the interlayer coupling strength at $T = 0$ K. $T_0 = \hbar v_F/2\pi k_B d$ is the characteristic temperature and d is the thickness of the spacer, over which the interlayer coupling strength monotonously changes with temperature. Malozemoff[64] has proposed that $H_{EX} \propto \sqrt{A_{AF}\, K_{AF}(0)}(1 - T/T_B)$, where A_{AF}, K_{AF} and T_B are the exchange constant, magnetocrystalline anisotropy and blocking temperature, respectively, of the AFM material. It is found that the interlayer coupling increases and the interfacial coupling decreases for an AFM insulator, but that both quantities decrease for an AFM metal with increasing temperature.

At low temperatures, the interfacial coupling dominates the couplings after a ZFC process. When the interfacial coupling is strong enough, the reversal of the Fe and Co layers

will occur simultaneously (Fig. 10(a)). With increasing temperature, the reduction of the interfacial coupling leads to the appearance of a step in the hysteresis loop along with a reduction of L. The enhancement of the interlayer coupling results in the gradual disappearance of both the step and the FM coupling at $T \geq 220$ K for the film with Cr_2O_3 and at $T \geq 310$ K for the film with NiO. For the FC case, strong FM coupling in FM/AFM will exist at low temperature. (See the negative exchange bias field in Fig. 10(a)). For the increasing field branch, the moments of the FM layers will reverse at a smaller field in order to reduce the interfacial energy (FM coupling in interface is in a low energy state). The stronger the exchange coupling in Co/Cr_2O_3 is, the more instable is the Co/Cr_2O_3 interface, which leads to moment reversal of the Co and Fe layers at the same field in Fig. 10(a).[59,65] In addition, a spin-flop-like phenomenon is noticed in the film with NiO at 100 K (and with Cr_2O_3 at 50 K). Some AF materials, in which a spin-flop phenomenon may occur, have a relatively weak interaction between spin moments.[66,67] In our system, three parts can thus be assumed as an AFM-like material when moments of the FM layers are antiparallel. Due to the relative weakness of the interlayer coupling between FM layers as compared with the FM anisotropy, a magnetic field applied along the direction parallel to the easy magnetization direction of FM layers may result in a spin-flop-like phenomenon (Fig. 8). For AFM insulating spacer, the interlayer coupling increases and the interfacial coupling decreases with increasing temperature. Therefore, there is a balance between these two couplings at a critical temperature (T_{cr}). At $T < T_{cr}$, the large L and small M_S are caused by the strong interfacial coupling between AFM and FM, which are also due to no orientation of magnetic moments at AFM/FM interface after ZFC. The interlayer coupling becomes dominant at $T > T_{cr}$, the FM interlayer coupling results in the increase of L and the decrease of M_S can be ascribed to the thermal effect. As a result, the temperature of the maxima of L and minima of M_S after ZFC corresponds to this critical temperature in Figs. 11(a) and 4(b).

Because a strong competition between interlayer and interfacial coupling has been observed in FM/AFM/FM trilayers with AFM metallic and insulating spacer materials,[58,68] effects of the AFM spacer thickness and magnetic anisotropies of FM layers on the exchange coupling in FM/AFM/FM trilayers have been investigated. However, in FM/AFM/FM systems, the constant FM layers had been used in all previous work to investigate the variation of the exchange coupling upon changing the AFM spacer thickness. This encouraged us to study the role of different FM layers on the interfacial and interlayer coupling in trilayers. We reported the observation of temperature dependence of exchange coupling in FM/Cr_2O_3/FM trilayers with FM Co, Fe, $Ni_{80}Fe_{20}$ layers.[69]

Figure 12 shows magnetic hysteresis loops at 50 K (a), 150 K (c), 225 K (e), of Co (3 nm)/Cr_2O_3 (3 nm)/Fe (10 nm) and at 50 K (b), 200 K (d), 350 K (f), of Co (3 nm)/Cr_2O_3 (25 nm)/ Fe (10 nm) after ZFC. It is found from Fig. 12(a) that the hysteresis loop exhibits good coupling between FM layers across the AFM spacer at 50 K. At 150 K, a step of magnetization (M_P) appears and then it jumps to saturation magnetization M_S at the saturation field (H_S). (M_P and H_S are indicated by arrows in Fig. 12(c)). Moreover, the disappearance of the step at $T \geq 225$ K indicates the FM coupling between two FM layers. However, it is found that magnetization increases with increasing H in the first quadrant (symmetry in the third quadrant) with $M_P = 0.36$ at 50 K for $t = 25$ nm in Fig. 12(b), while the fact that no clear FM coupling is observed even at $T \geq 350$ K suggests quite weak interlayer coupling for this sample. The magnetic moment per Fe atom is 2.22 μ_B and per Co atom is 1.72 μ_B. For the antiparallel alignment of the moments of two FM layers, the M_P is about 0.6. For a sample with $t = 25$ nm, the values of $M_P = 0.36$ at 50 K and $M_P \approx 0.6$ at $T \geq 200$ K mean the partial reversal of Fe layer and the Fe and Co layers becoming antiparallel at the step, respectively.

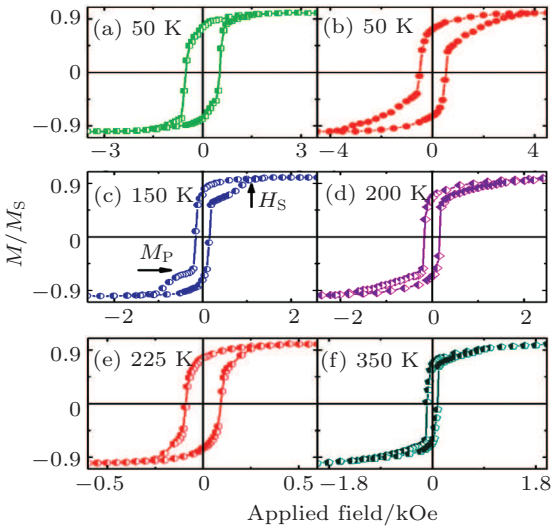


Fig. 12. Magnetic hysteresis loops at 50 K (a), 150 K (c), 225 K (e), of Co (3 nm) /Cr_2O_3 (3 nm) /Fe (10 nm) and at 50 K (b), 200 K (d), 350 K (f), of Co (3 nm) /Cr_2O_3 (25 nm) /Fe (10 nm) after ZFC.[69]

The hysteresis loops at 10 K of trilayers with different spacer thicknesses 3 nm, 6 nm, 15 nm, and 25 nm after ZFC (solid symbol) and FC (open symbol) are presented in Fig. 13(a)–13(d), respectively. It is found that two FM layers are well coupled after ZFC for the trilayers with spacer thickness of 3 nm and 6 nm. But the steps are clear for $t = 15$ nm and 25 nm, indicating weak interfacial coupling between the AFM and FM layers for a thicker spacer. For the FC case, all the trilayers exhibit steps in the third quadrant with different values of H_S and no step in the first quadrant. H_S in the third quadrant is defined as H_{S3} and in the first quadrant H_{S1} (as

arrows indicate). The asymmetrical coefficient $L = H_{S3}/H_{S1}$ is defined. $L = 1$ means symmetrical loops, suggesting that the interfacial coupling between FM and AFM layers is quite weak after FC.[59]

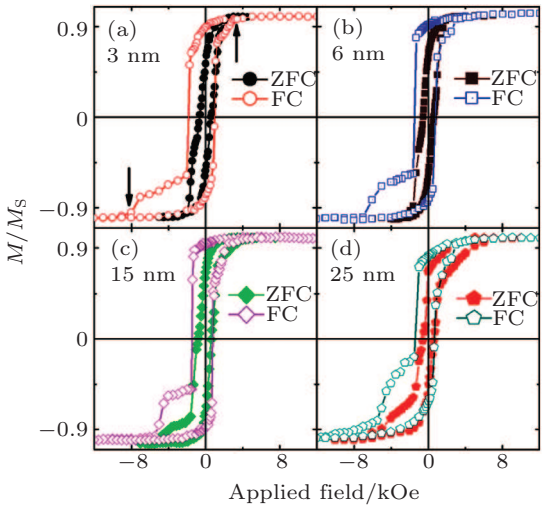


Fig. 13. Magnetic hysteresis loops at 10 K for $t = 3$ nm (a), 6 nm (b), 15 nm (c) and 25 nm (d) after ZFC and FC, of Co (3 nm) /Cr_2O_3 (t) /Fe (10 nm).[69]

The curves of L versus T with spacer thickness of 3, 6, 15 nm are presented in Fig. 14. Note that the values of L decrease with increasing spacer layer at low T, indicating stronger interfacial coupling for a thinner spacer, moreover, $L \approx 1$ for $t = 15$ nm at the lower temperature also confirms weaker interfacial coupling for a thicker spacer layer.

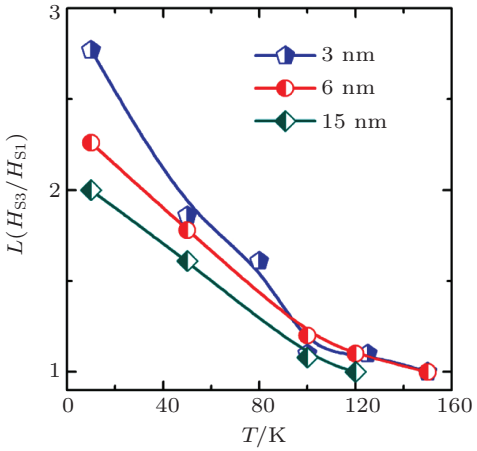


Fig. 14. Temperature dependence of asymmetrical coefficient L for samples with $t = 3$ nm, 6 nm and 15 nm.[69]

To further clarify the relationship between magnetization orientation of FM layers and spin-dependent scattering magnetoresistance (MR), the resistance (R) and magnetic hysteresis loops for 3 nm after FC are shown in Fig. 15. Negative MR is observed at the coercivity field in Fig. 15(c) and the sharp decrease/increase of R corresponds to the first/second sharp switching in the hysteresis loop, respectively. In Fig. 15(a), the plateau of R corresponds to the step of the field-decreasing branch in the third quadrant and the second minimum of R corresponds to magnetization reversal in the Co layer at about -8 kOe. However, it is clear from Figs. 15(b) and 15(d) that the two plateaus of R corresponding to the two steps in the hysteresis loop are different from those at 10 K, suggesting the strong influence of interfacial exchange coupling on the spin-dependent scattering. The interlayer coupling (sign and strength) between the Co and Fe layers can be determined by minor-loop measurements (as shown in Fig. 15(b)). The minor-loop shift $H_E < 0$ means the FM coupling, while $H_E > 0$ is indicative of the AFM coupling and the interlayer coupling strength of the trilayers can be expressed as $J_E = H_E M_S t_{FM}$,[60] where M_S and t_{FM} are the saturation magnetization and the thickness of the Fe layer, respectively. All the values of $H_E < 0$ mean the FM coupling between FM layers for all the trilayers and small values of H_E mean weak interlayer coupling strength in trilayers in the temperature range.

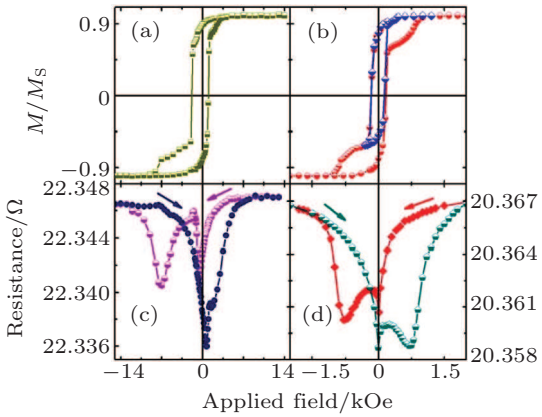


Fig. 15. Magnetic loop at 10 K (a), the major and minor loops at 150 K (b), the R–H curve at 10 K (c) and R–H curve at 150 K, of Co (3 nm)/Cr_2O_3 (3 nm) /Fe (10 nm) after FC.[69]

The temperature dependence of M_S after ZFC and FC for $t = 25$ nm, 15 nm, and 3 nm and saturation R after ZFC (nearly the same values of saturation R for ZFC and FC cases) for $t = 3$ nm are presented in Fig. 16. As M_S is largest after FC at 10 K for each sample, each curve of Fig. 16 is normalized by M_S after FC at 10 K. It is found that the value of M_S for every sample after ZFC exhibits a peak at different temperatures (as arrows indicated), but it decreases with increasing temperature for every one after FC. Meanwhile, the peak temperature (T_P) of the ZFC curve shifts to low temperature with increasing spacer thickness. In Figs. 16(c) and 16(d), the maximum of M_S after ZFC corresponds to the minimum of saturation R at T_P, indicating that the competition between interfacial coupling between FM and AFM layers and interlayer coupling between the two FM layers greatly influence the magnetotransport properties of trilayers. The experimental results at low bias are generally interpreted according to Jullière's expression, $\Delta R/R = (R_{AP}–R_P)/R_{AP} = 2P_1P_2/(1 + P_1P_2)$, where

R_{AP} and R_P are the resistances in the antiparallel and parallel states, respectively and P_1 and P_2 are the electron spin polarizations of the two electrodes.[70] The negative magnetoresistance presented in Fig. 15 is indicative of the different signs of the electron spin polarizations of Co and Fe electrodes. Moreover, the values of R in Figs. 15(c) and 15(d) indicate that the interfacial coupling and interlayer coupling greatly affect the magnetotransport properties of trilayers.

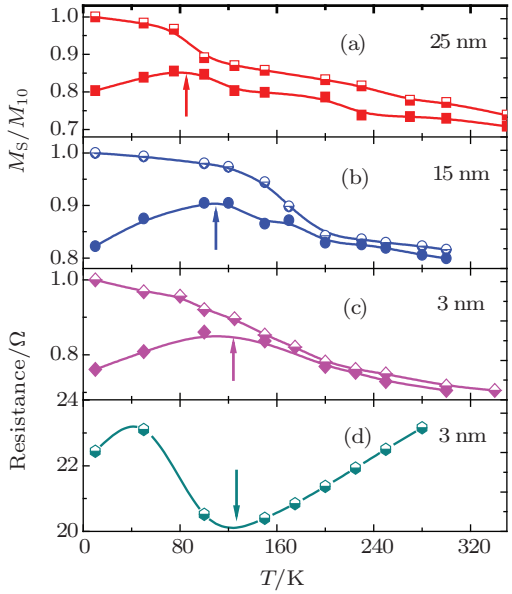


Fig. 16. Temperature dependence of saturation magnetization for t = 25 nm, 15 nm and 3 nm after ZFC and FC and saturation R for 3 nm after ZFC, respectively, of Co (3 nm) /Cr_2O_3 (t) /Fe (10 nm). The arrow indicates the peak temperature of ZFC curve and saturation R.[69]

5. Effects of magnetic anisotropy on the exchange coupling and magnetotransport properties

A strong competition between two kinds of coupling, i.e., the interfacial coupling between two interfaces and the interlayer coupling between two FM layers across the AFM layer, has been observed in FM/AFM/FM trilayers with AFM a metallic or insulating spacer.[68] It was reported that the FM properties are greatly affected by the underlayer in $[Pt/Co]_3$/NiO/$[Pt/Co]_3$ multilayers,[60] and a similar phenomenon was observed also in other systems.[71] However, most previous work has been focused on trilayers with the same FM layers and it has seldom been reported that the exchange coupling is influenced by the order of different FM layers. In this section, we summarize our report on the effects of magnetic anisotropy on the exchange coupling of Fe/NiO/Co and Co/NiO/Fe trilayers and magnetotransport properties of these two trilayers.[72]

Trilayers Co (3 nm)/NiO (6 nm)/Fe (10 nm) (A), Fe (10 nm)/NiO (6 nm)/Co (3 nm) (B) and bilayers Co (3 nm)/NiO (6 nm) (C), NiO (6 nm)/Fe (10 nm) (D), Fe (10 nm)/NiO (6 nm) (E), NiO (6 nm)/Co (3 nm) (F) were prepared by DC and RF magnetron sputtering at room temperature on an Si (100) substrate with Ag (10 nm) sublayer and Ag (5 nm) cover layer. The substrate, sublayer and cover layer in all these trilayers and bilayers are the same so that we do not mention Si (100)/Ag (10 nm)/···/Ag (5 nm) in the following text. The hysteresis loops at 10 K of trilayer A, after field-cooling (FC) in 2 kOe and zero-field-cooling (ZFC) and of trilayer B, after FC in 2 kOe, are shown in Fig. 17. It is clear that after FC, a step in the third quadrant is found for each trilayer. Moreover, a larger step in magnetization (M_P) is observed for trilayer A (as the arrow indicates). The difference between the two M_P values is defined as ΔM_P. The inset in Fig. 17 presents the negative-field part of the M–H loops recorded at 100 K after FC for the trilayers A and B. No clear step is found for B at 100 K.

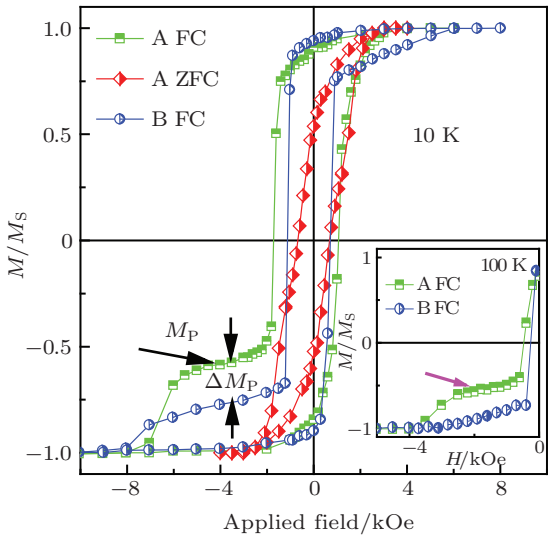


Fig. 17. Hysteresis loops at 10 K of the trilayers Co (3 nm)/NiO (6 nm)/Fe (10 nm) (A) after FC in 2 kOe and ZFC and Fe (10 nm)/NiO (6 nm)/Co (3 nm) (B) after FC in 2 kOe. Inset: M–H loops in negative field of A and B after FC at 100 K.[72]

The M–H loops of the bilayers C, D, E, and F have been recorded at 10 K after FC (Fig. 18). It is found that the coercivity (H_C) and the exchange-bias field (H_E) are different for all of them,[73] which indicates that the sublayer strongly affects the magnetic anisotropy and further influences the interfacial coupling of the bilayers.[74] At high temperatures, the M–H loops of trilayers A and B exhibit good coupling, when the H_C values of two FM/AFM of the trilayers are equal to each other, or when the FM interlayer coupling between two FM layers dominates. To make this clear, the negative-field parts of the M–H loops at 290 K of the bilayers E and F are shown in the inset of Fig. 18. The H_C of 0.075 kOe for the former and 0.16 kOe for the latter confirms the domination of interlayer coupling at high temperatures.

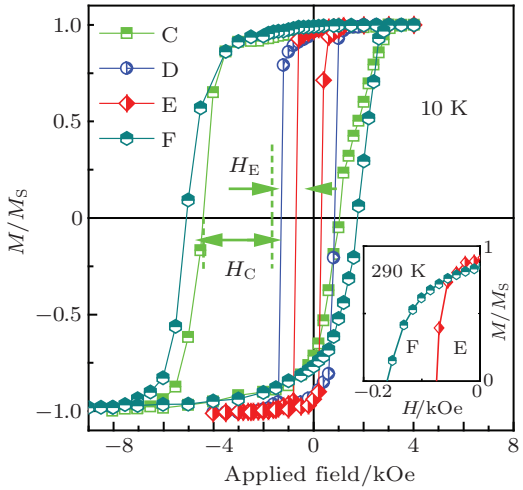


Fig. 18. *M–H* loops at 10 K of the bilayers Co (3 nm)/NiO (6 nm) (C), NiO (6 nm)/Fe (10 nm) (D), Fe (10 nm)/NiO (6 nm) (E) and NiO (6 nm)/Co (3 nm) (F) after FC. Inset: *M–H* loops at 290 K in negative field of the bilayers E and F.[72]

To study the temperature dependence of the magnetic properties of the trilayers, the saturation magnetization (M_S) of the trilayers A and B after ZFC are presented in Fig. 19. All M_S values are normalized to the 200-K value for each sample. It is noticed that the variation of M_S with temperature is similar for the two trilayers and that M_S increases from 10 K to 200 K and then decreases with further increasing temperature. The inset of the figure shows clearly that ΔM_P increases with increasing temperature from 0.19 at 10 K to 0.42 at 200 K.

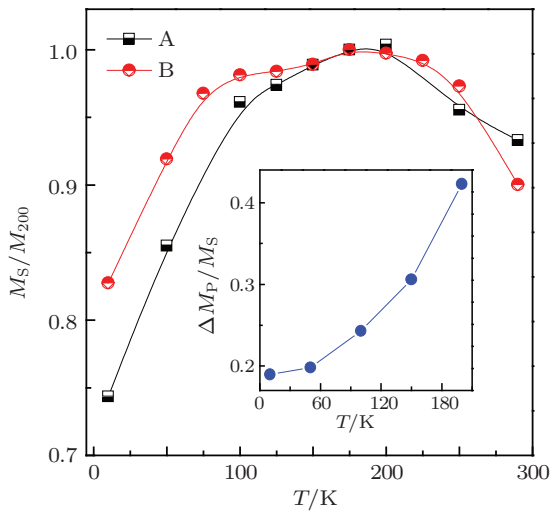


Fig. 19. The saturation magnetization M_S normalized to the value at 200 K of the trilayers A and B after ZFC. Inset: The $\Delta M_P/M_S$ versus temperature.[72]

To further clarify the relationship between the magnetization orientation of the FM layers and the magnetoresistance (MR), the *R–H* curves of trilayer A recorded after FC and ZFC at 10 K are presented in Figs. 20(a) and 20(b). It is interesting to notice that MR is negative for ZFC but positive for FC. This indicates that the applied field changes the sign of the FM spin polarization (P) in the trilayers. In Figs. 20(a) and 20(b), the fields corresponding to maximum or minimum R values (indicated by the dashed arrows) are consistent with the moment reversals of Fe and Co in Fig. 17.

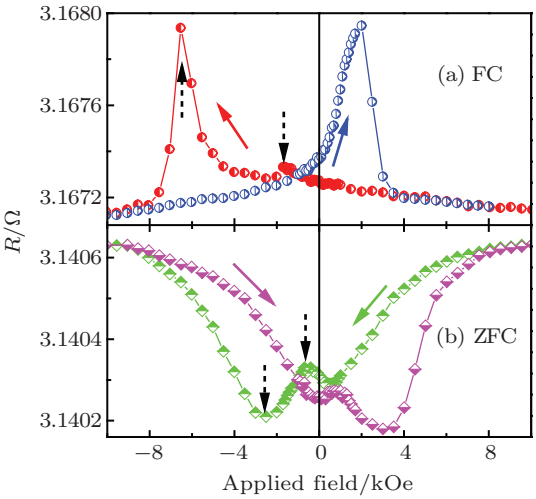


Fig. 20. *R–H* curves at 10 K for trilayer A after FC (a) and ZFC (b).[72]

The temperature dependence of the magnetotransport properties of bilayer E after ZFC and FC and trilayers A and B after ZFC is presented in Fig. 21. For convenience, all values of R have been normalized to the value at 295 K. The inset of the figure presents the *R–T* curves of trilayer A after ZFC and FC in fields of 2 kOe and 10 kOe. As can be seen in Fig. 21, the temperature corresponding to the minimum R (T_m) has nearly the same value of about 245 K for the ZFC trilayers A and B, whereas T_m is about 175 K for the ZFC and FC of bilayer E. Furthermore, T_m shifts to lower temperatures in an applied field, as shown in the inset of Fig. 21.

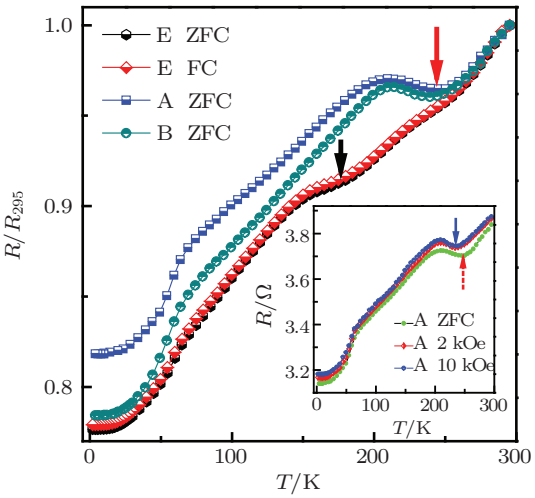


Fig. 21. *R–T* curves for the bilayer E after ZFC and FC and the trilayers A and B after ZFC. Inset: *R–T* curves for trilayer A after ZFC and FC in zero field, and at 2 kOe and 10 kOe.[72]

The change of the total energy with changing temperature arises mainly from the interfacial and interlayer exchange coupling in the FM/NiO/FM trilayers.[58] Because

they have the same FM and AFM layers, the interlayer coupling between the FM layers can be considered to be the same in the trilayers A and B. We now focus on the interfacial coupling in FM and AFM layers with changing temperature. The interfacial-coupling energy decreases with increasing temperature.[64,75] The interlayer-coupling strength is given by $J(T) \propto (T/T_0)/\sinh(T/T_0)$, and increases with increasing temperature.[68]

At low temperatures, the interfacial coupling is quite strong and the interfacial coupling in the bilayers in Fig. 18 is consistent with that in the trilayers in Fig. 17. The value of M_P of about 0.6 for trilayer A in Fig. 17 indicates antiparallel moments of Fe and Co.[59] However, the larger M_P value for trilayer B in Fig. 17 may be due to a divided Co layer, in which some moments of Co will reverse with reversal of the Fe layer at first, while the reversal of the other moments occurs at a larger field. Furthermore, with increasing temperature, the increase of ΔM_P results from weaker interfacial coupling in B than in A. As the interfacial coupling decreases and the interlayer coupling increases with increasing temperature, the temperature of the maximum of M_S in Fig. 19 corresponds to the balance temperature of the two types of couplings.[58]

The experimental results at low bias are generally interpreted in terms of Jullière's expression, $\Delta R/R = (R_{AP}-R_P)/R_{AP} = 2P_1P_2/(1+P_1P_2)$, where R_{AP} and R_P are the resistances in the antiparallel and parallel states, respectively and P_1 and P_2 are spin polarizations of the two electrodes.[70] The change of sign of MR in Fig. 20 after FC is due to the reversal of P in an applied field. Figures 20(a) and 20(b) confirm that P of Co reverses with increasing applied field. Moreover, T_m in Fig.21 is the T_B of NiO, due to the disappearance of exchange bias in trilayers around T_m. The decrease of T_m originates in the enhancement of the T_B of AFM by interfacial coupling; and the phenomenon of nearly no difference of R after ZFC and FC in bilayer E originates from weak interfacial coupling in Fe/NiO.[59] In addition, the T_B of AFM can be greatly affected by an applied field, shifting to a lower temperature in larger field,[76] and this is why T_m shifts to a lower temperature as seen in the inset of Fig. 21. The low-temperature behavior of R can be expressed as $R = R_0 + \alpha T^\gamma$, where γ is the exponent parameter,[77] and the $R \propto T^3$ may be due to the large amount of disorder in our system.[78]

6. Tuning interfacial exchange coupling in FM/FM/AFM heterostructures with in-plane and out-of-plane easy axes

The EB is usually obtained by magnetic field cooling FM/AFM bilayers through the Néel temperature of the AFM material or depositing FM/AFM bilayers in the presence of a magnetic field. In most cases, the EB is observed in FM/AFM bilayers with in-plane anisotropy, but in a few cases it is also seen with out-of-plane anisotropy.[60,79] In FM/AFM/FM structures with orthogonal easy axes, using element-specific X-ray magnetic circular dichroism, Nogués *et al.* demonstrated that in-plane and out-of-plane EB can be induced simultaneously by using a single antiferromagnet and ZFC, whereas the FC process induces EB only to the layer with an easy axis parallel to the direction of the cooling field.[80] Coupling FM/FM layers with distinct anisotropy directions has already been proven to be an alternative solution to obtain EB.[81–83] By means of in-plane saturation, the formation of uncompensated moments in a [Pt/Co] multilayer or TbCo layer with out-of-plane anisotropy leads to a shift of the hysteresis loop of an adjacent NiFe thin film with in-plane anisotropy without the need for annealing at high temperature. Recently, Yang *et al.*[84] demonstrated EB-like behavior in a dual spin valve of [Pd/Co]/Cu/Co/Cu/[Co/Pd] by magnetostatic coupling in the absence of AFM layer. Based on the above-mentioned structures (FM/AFM, FM/FM, FM/AFM/FM), we designed an FM/FM/AFM heterostructure $[Pt/Co]_n$/NiFe/NiO, in which two FM layers have out-of-plane and in-plane anisotropy, respectively, to tune the EB by applying different in-plane magnetic fields and different cooling procedures.[85] The FM/FM interface may induce EB isothermally and reversibly along the applied field direction, while the FM/AFM interface can pin the magnetic moments by FC. Therefore, the EB in the present heterostructure can be tuned by the combination of these two effects.

The out-of-plane hysteresis loops at room temperature of the $[Pt/Co]_5$/NiFe (t_{NiFe})/NiO (5 nm) heterostructures with t_{NiFe} are shown in Fig. 22. For $t_{NiFe} = 2$ nm, the figure shows a rectangular hysteresis loop, which indicates that the magnetization reversal takes place by domain nucleation at first, followed by rapid motion of the domain walls. For $t_{NiFe} = 5$ nm [Fig. 22(a)], the hysteresis loop is the overlapping of two loops: one hard-axis loop corresponding to the NiFe layer with in-plane anisotropy and one square loop corresponding to the $[Pt/Co]_5$ multilayers (ML). After saturation, the moments of all layers in the heterostructure are perpendicular to the film plane. With a decrease in the magnetic field, the moment of the NiFe layer first rotates from the out-of-plane direction to the in-plane direction and then the moment of the $[Pt/Co]_5$ ML reverses abruptly at an applied field of -470 Oe [Fig. 22(b)]. With increasing t_{NiFe}, $H_C^{\parallel}$ and M_r/M_s both decrease simultaneously and the switching field distribution (SFD) becomes broader as well (as shown in insets of Fig. 22), which indicates that the exchange interaction and the magnetization reversal process of the heterostructures vary with NiFe thickness.

A magnetic field between -3 kOe and 3 kOe, which is sufficient to saturate the in-plane NiFe layer, as shown in Fig. 23(c), but not large enough to saturate the $[Pt/Co]_5$ ML,

as shown in the inset of Fig. 23(c), has been applied to measure the in-plane minor hysteresis loops at 10 K. The in-plane minor hysteresis loops of the $[Pt/Co]_5$/NiFe (5 nm) layers at 10 K are shown in Fig. 23(a). After application of saturation field of 20 kOe and −20 kOe, the in-plane minor hysteresis loops shift along negative and positive directions, and an enhanced coercivity (H_C) is found. The presence of the vertical shift ΔM (i.e., the difference between the positive and negative saturation magnetizations) indicates that an in-plane net uncompensated moment from the $[Pt/Co]_5$ ML is induced by applying the in-plane saturation field.[86] The coexistence of EB and vertical shift indicates the role of uncompensated spins on the EB. The uncompensated moments result from unequally oriented closure domains at the $[Pt/Co]_5$/NiFe interface, which is similar to the case of the uncompensated spins in conventional FM/AFM structures.[87] Due to FM exchange coupling, the hysteresis loop shifts along the field axis and H_C increases. So, the in-plane EB in $[Pt/Co]_5$/NiFe (5 nm) is reversible after applying a magnetic saturation field in the opposite direction; this is one way to manipulate the EB, contrasting with that in conventional AFM/FM bilayers.

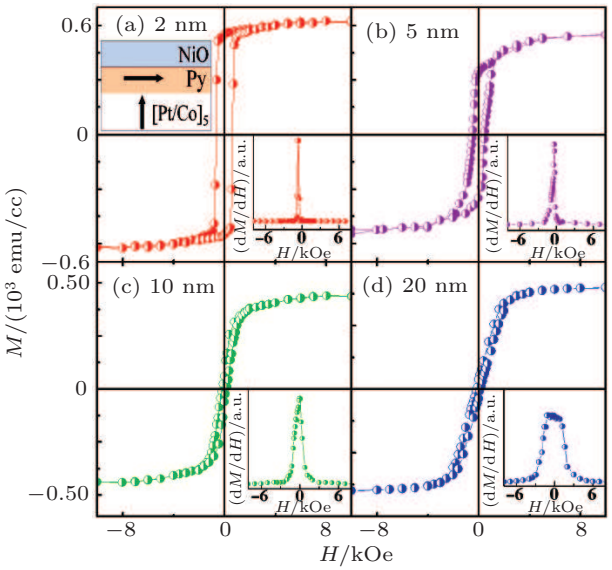


Fig. 22. Out-of-plane hysteresis loops at 295 K for $[Pt/Co]_5$/NiFe (t_{NiFe})/NiO (5 nm) heterostructures. The inset in Fig. 22(a) is a sample schematic diagram. Inset in (a)–(d): the first derivative of the hysteresis loops.[85]

To tune the EB, the in-plane minor hysteresis loops at 10 K after FC for the $[Pt/Co]_5$/NiFe (5 nm)/NiO (5 nm) heterostructure are shown in Fig. 23(b). The in-plane EB field ($H_E^{\parallel}$) of −160 Oe is found after FC and increases to −240 Oe after application of a magnetic field of 20 kOe. Then the $H_E^{\parallel}$ changes to +80 Oe after application of a −20 kOe magnetic field. The reversible exchange coupling at the $[Pt/Co]_5$/NiFe (5 nm) interface and the irreversible exchange coupling at the NiFe (5 nm)/NiO (5 nm) interface cause different $H_E^{\parallel}$ after application of in-plane saturation fields of 20 kOe and −20 kOe, respectively. The $H_E^{\parallel}$ of the ZFC minor hysteresis loop (−180 Oe) is a little smaller than that of the FC minor hysteresis loop, as shown in the inset of Fig. 23(b). The difference in $H_E^{\parallel}$ for the ZFC and FC cases originates from the exchange coupling at the NiFe/NiO interface. In ZFC, the EB is mainly induced by the exchange coupling between the uncompensated in-plane moments of the $[Pt/Co]_5$ ML and the NiFe layer. For FC, the EB is induced by both exchange coupling in traditional AFM/FM bilayers (NiFe/NiO) and exchange coupling between the uncompensated in-plane moments of the $[Pt/Co]_5$ ML and the moments of the NiFe layer. With temperature increasing above a certain value, the contribution from exchange coupling at the NiFe/NiO interface disappears and the difference in $H_E^{\parallel}$ for ZFC and FC may be erased. To confirm this, the $H_E^{\parallel}$ values for ZFC and FC at different temperatures are given in Fig. 24. Below 120 K, the $H_E^{\parallel}$ for FC is larger than that for ZFC. Above 120 K, the $H_E^{\parallel}$ values for FC and ZFC are nearly the same. So, there is a transition temperature at 120 K, which may result from the in-plane blocking temperature (T_B) of the NiO layer.[88] Below T_B, the $H_E^{\parallel}$ for FC is enhanced by the exchange coupling at the NiFe/NiO interface. Moreover, the EB in this heterostructures is still maintained at room temperature, which is useful in industrial applications.

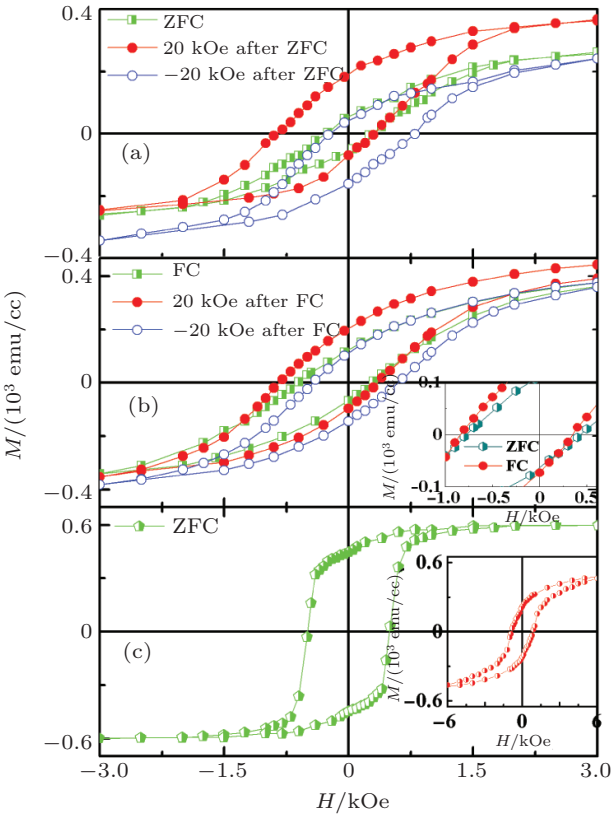


Fig. 23. In-plane minor hysteresis loops at 10 K for (a) $[Pt/Co]_5$/NiFe (5 nm), ZFC (square), saturated with 20 kOe (solid circle) and −20 kOe (open circle) after ZFC. (b) $[Pt/Co]_5$/NiFe (5 nm)/NiO (5 nm) after 3 kOe FC (square), saturated with 20 kOe (solid circle) and −20 kOe (open circle) after 3 kOe FC. Inset: enlarged view of ZFC and FC at 10 K after saturated with 20 kOe. (c) In-plane loop at 10 K for NiFe/NiO bilayers after ZFC. The inset: the in-plane loop of $[Pt/Co]_5$/NiFe (5 nm) at 10 K.[85]

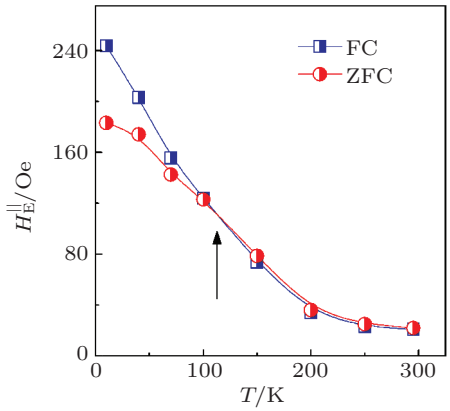


Fig. 24. Temperature dependence of in-plane $H_E^{\parallel}$ at 10 K of FC (squares) and ZFC (circles) for $[Pt/Co]_5$/NiFe (5 nm)/NiO (5 nm) heterostructures. The data were measured after applying 20 kOe at 10 K following ZFC and FC processes, respectively.[85]

The in-plane set magnetic field ($H_{set}^{\parallel}$) dependence on $H_E^{\parallel}$ is presented to further clarify the influence of $[Pt/Co]_n$ ML on the magnetic properties of the heterostructures, as shown in Fig. 25. For $H_{set}^{\parallel} < 6$ kOe, the $H_E^{\parallel}$ and $H_C^{\parallel}$ keep nearly constant. For $H_{set}^{\parallel} > 6$ kOe, the $H_E^{\parallel}$ and $H_C^{\parallel}$ increase abruptly and reach a plateau. When $H_{set}^{\parallel}$ is smaller than 6 kOe, the EB originates mainly from the exchange coupling in the FM/AFM layers. When $H_{set}^{\parallel}$ is larger than the anisotropy field of the $[Pt/Co]_5$ ML, a net uncompensated moment in the $[Pt/Co]_5$ ML is induced at the interface of the $[Pt/Co]_5$/NiFe layers after the removal of the set field. The increase in $H_E^{\parallel}$ with $H_{set}^{\parallel}$ can be attributed to the exchange coupling between the uncompensated in-plane moments of the $[Pt/Co]_5$ ML and the NiFe layer. Therefore, in this heterostructure, the EB can be tuned isothermally by applying different $H_{set}^{\parallel}$, even after the appearance of an established EB after FC.

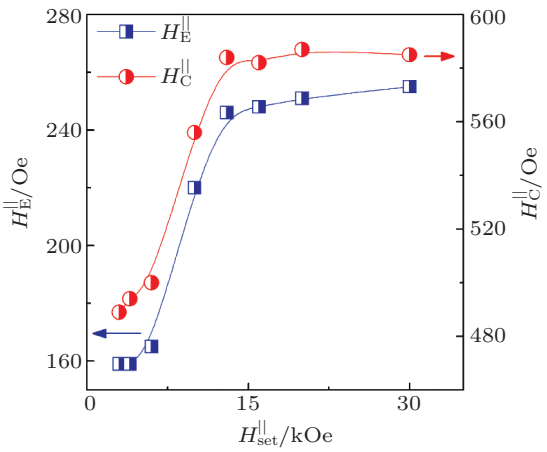


Fig. 25. In-plane set magnetic field dependence of in-plane $H_E^{\parallel}$ and $H_C^{\parallel}$ for $[Pt/Co]_5$/NiFe (5 nm)/NiO (5 nm) heterostructures at 10 K after FC at 3 kOe.[85]

The dependence of the $H_E^{\parallel}$ and $H_C^{\parallel}$ at 10 K on the thickness of the NiFe layer of $[Pt/Co]_5$/NiFe (t_{NiFe})/NiO (5) heterostructures is shown in Fig. 26. The $H_E^{\parallel}$ decreases with increasing t_{NiFe}, which is similar to the conventional EB structures described by the phenomenological formula $H_E = \Delta\sigma/M_{FM}t_{FM}$,[89] where $\Delta\sigma$ is the interfacial exchange coupling energy and M_{FM} and t_{FM} are the saturation magnetization and thickness of the NiFe layer, respectively.

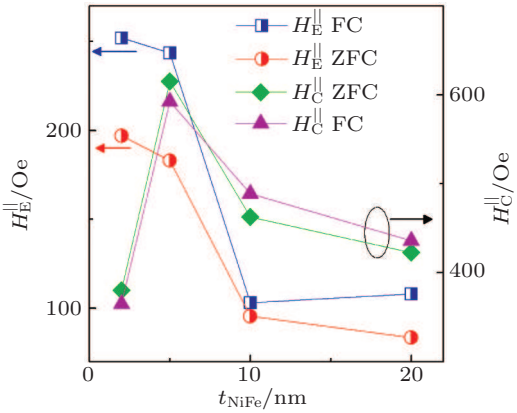


Fig. 26. NiFe thickness dependence of in-plane $H_E^{\parallel}$ and $H_C^{\parallel}$ for $[Pt/Co]_5$/NiFe (t_{NiFe})/NiO (5) heterostructures at 10 K after saturated with 20 kOe following ZFC and FC process.[85]

7. Exchange coupling and magnetotransport properties in FM/AFM and FM/AFM/FM antidot arrays

As the dimensions of nanostructured magnetic materials become comparable to the characteristic length scales of physical phenomena (e.g., domain-wall width, exchange length, and spin-diffusion length), their magnetic and magnetotransport properties will be different from continuous films.[90,91] Various routes, such as electron-beam lithography,[92] block copolymer templates,[93] and nanoporous ZrO_2 membranes,[94] have been used to fabricate patterned magnetic nanostructures at submicron dimensions. Among these nanofabrication methods, an easy and low-cost way is to deposit magnetic materials onto porous anodic aluminum oxide (AAO) templates. It has been reported that for antidot arrays, which consist of an array of pores in the films, the coercivity field H_C and the EB field H_E are enhanced.[95] However, the opposite has been reported: that in CoFe/IrMn EB nanostructure, H_E can be either enhanced due to the pinning of AFM spins or suppressed because of the misalignment of AFM and FM spins at the edge of the pores, depending on the pore density.[96] The interfacial FM/AFM exchange coupling can be strongly affected by the antidot arrays, in comparison with the continuous films. Wang *et al.*[97] also found that the current density distribution is periodically modulated by the presence of holes, which gives rise to the interesting behavior of the magnetoresistance (MR). Much work has focused on the properties of antidot arrays for FM layers or FM/AFM bilayers,[98,99] and intensively investigated

the exchange coupling in FM/AFM/FM continuous films because of its physical significance.[12,58] However, the exchange coupling in FM/AFM/FM antidot arrays has seldom been reported. We investigated the influence of FM layer thickness and thermal-activation effects on EB phenomenon in Co/NiO antidot arrays and continuous films,[100] and the magnetic and magnetotransport properties in Co/NiO/Fe antidot arrays.[101] It was found that the EB field H_E in the Co/NiO antidot arrays can be either larger or smaller than that in the continuous films, depending on the FM thickness. In addition, the blocking temperature of the antidot arrays is higher than that of the continuous films. These results can be explained by an anisotropy distribution in the FM/AFM layer, which has been modified by the membranes. In the Co/NiO/Fe trilayers, anomalous magnetic and magnetotransport properties, in particular a positive MR, are observed for the antidot arrays, but a negative MR is found in the continuous films, which is due to the spin polarization changed by the formation of the antidot arrays. The larger resistance and clear variation of resistance at low temperatures may be due to the stronger spin scattering and higher additional interface resistance in the antidot arrays.

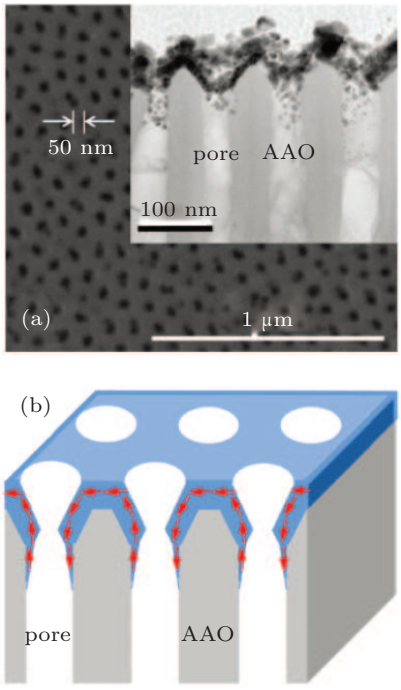


Fig. 27. (a) SEM image of Ag (10 nm)/Co (8 nm)/NiO (5 nm)/Ag (5 nm) antidot arrays. Inset: cross-sectional TEM image of the antidot arrays. (b) Three-dimensional sketch of the antidot arrays, the arrows indicate the magnetization direction of magnetic films.[100]

Nanoporous AAO templates made by anodizing high-purity aluminum foils in a two-step anodization process in a sulfuric acid solution with pore depth of 30 μm, Si (001) and Al_2O_3 (0001) were used as substrates.[102] Ag (10 nm)/Co (t_{Co})/NiO (5 nm)/Ag (5 nm) antidot arrays on AAO templates and the corresponding continuous films on Si and Al_2O_3 substrates were prepared by high-vacuum magnetron sputtering. A scanning electron microscope (SEM) image of Ag (10 nm)/Co (8 nm)/NiO (5 nm)/Ag (5 nm) an antidot array is shown in Fig. 27(a). The pore diameter is about 40 nm and the edge-to-edge spacing about 50 nm. Due to the high aspect ratio (pore depth/diameter), a sawtooth shape of the films is found. The cross-sectional TEM image in the inset of Fig. 27(a) shows that the materials are mainly deposited on the top and the inner wall of the templates and they do not reach the bottom of the pores. Figure 27(b) presents a three-dimensional sketch of the films deposited on top of the AAO templates. The directions of the FM and AFM moments at the edge and at the inner wall of the nanopores deviate from the in-plane direction.

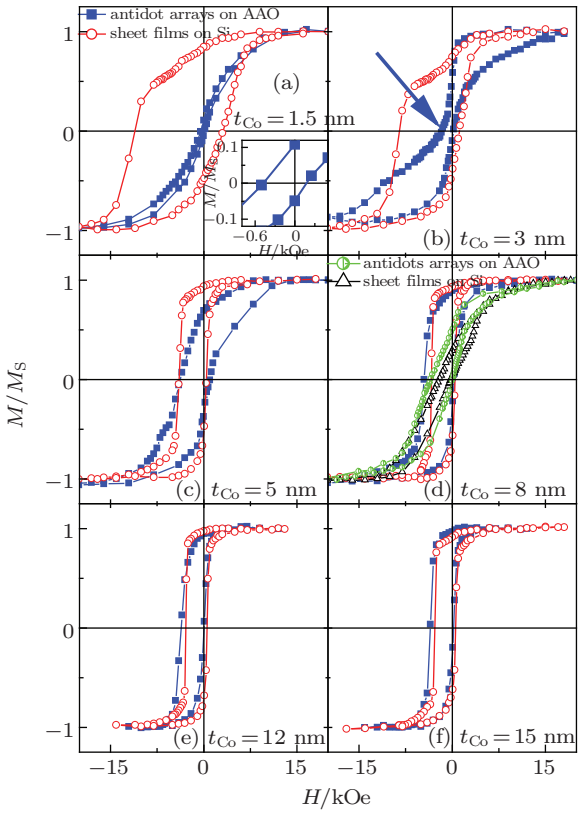


Fig. 28. (a)–(f) In-plane hysteresis loops of Ag (10 nm)/Co (t_{Co})/NiO (5 nm)/Ag (5 nm) antidot arrays on AAO substrates (solid squares) and continuous films on Si (open circles) with t_{Co} = 1.5, 3, 5, 8, 12, 15 nm. Inset in (a): enlarged view of hysteresis loop of antidot arrays with t_{Co} = 1.5 nm. The two additional hysteresis loops in Fig. (c): out-of-plane hysteresis loops of antidot arrays (half-filled circle) and of continuous films on Si (open triangle).[100]

A small shoulder appears in the descending branch of the magnetization curves of the continuous films with $t_{Co} < 5$ nm, which may originate from the asymmetric magnetization reversal mechanism or reversal of a partly unbiased Co layer. As shown in Fig. 28(b), a small loop shift and a two-step magnetization reversal process are observed in the antidot arrays with t_{Co} = 3 nm, which suggests the three-dimensional magnetization effect in the antidot arrays. The hysteresis

loops of the films with antidot arrays are canted and more asymmetrical than those of the continuous films, which is another indication of the three-dimensional magnetization effect in the films, similar to that in Cu/Co/Cu trilayers deposited on nanoporous alumina membranes.[103] Magnetic moments along the inner wall of the nanopores are aligned perpendicular to the film plane, whereas the moments between the nanopores are aligned within the film plane, as sketched in Fig. 27(b).

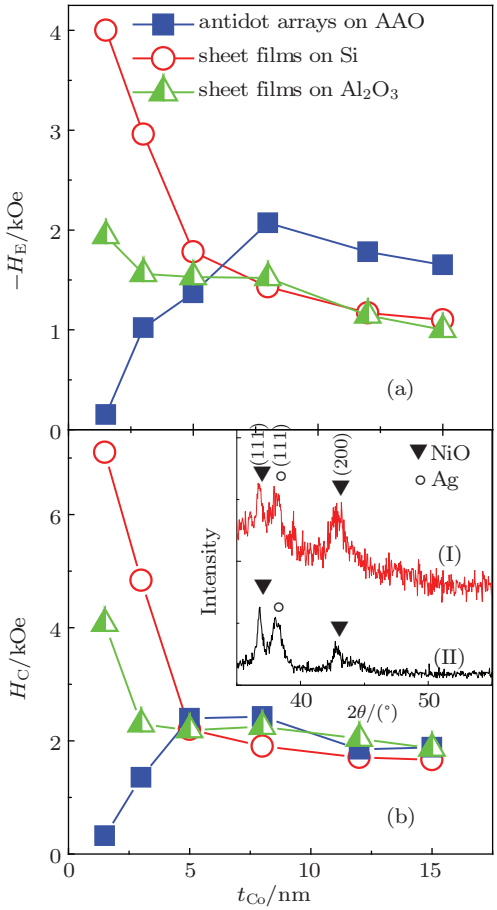


Fig. 29. Variation of H_E (a), H_C (b) with the Co thickness t_{Co} of the antidot arrays (solid squares); continuous films on Si and Al_2O_3 (open circles and triangles, respectively). Inset: XRD patterns of Ag (10 nm)/Co (8 nm)/NiO (5 nm)/Ag (5 nm) antidot arrays (I) and continuous films on Si (II).[100]

H_C and H_E of the continuous films both decrease with t_{Co} (Fig. 29), which is characteristic for EB continuous bilayers and thus suggests a mainly interfacial character of the FM–AFM coupling in the continuous films.[104] The substrates may affect the texture of Ag underlayer slightly and modify the anisotropy of the magnetic layers, which may induce the differences between the amplitudes of H_C and H_E for the continuous films on Si and Al_2O_3 substrates with $t_{Co} < 5$ nm. The larger H_C of the antidot arrays with $t_{Co} \geq 5$ nm, as compared with continuous films, can be attributed to domain-wall pinning in the vicinity of the nanopores.[98,105] With increasing Co thickness, the H_E of the antidot arrays increases, reaching a maximum at $t_{Co} = 8$ nm and then decreases with further increasing t_{Co}. In addition, for $t_{Co} > 5$ nm, H_E of the antidot arrays is larger than the H_E of the continuous films, which is attributed to pinning in the antidot arrays. However, for $t_{Co} \leq 5$ nm, H_E of the antidot arrays is smaller than that for the continuous films, which is due to the misalignment of FM and AFM spins at the edge and wall of the nanopores. For both the continuous films and the antidot arrays with $t_{Co} = 8$ nm, the out-of-plane EB field H_E is smaller than the in-plane EB field H_E (Fig. 28). XRD results in the inset of Fig. 29(b) show the NiO (111) texture in the antidot arrays and the continuous films. Using values for the exchange stiffness $A_2 = 6.7 \times 10^{-7}$ erg/cm (1 erg = 10^{-7} J) for the next-nearest neighbors and using the magnetic anisotropy constants $K_2 = 1.5 \times 10^5$ erg/cm^3 parallel to the (111) plane,[106] the AFM domain-wall width parallel to the (111) plane can be estimated to be $\delta_{AF} = \pi (A_2/K_2)^{1/2} = 66$ nm. When the films are deposited on the AAO templates, the nanopores reduce the domain size of NiO, which results in a larger interface exchange coupling. According to the random-field model,[64] the domain size is mainly determined by an FM exchange interaction within the FM layer and the random field acting on the AFM layer due to interfacial exchange coupling. In this static model, the exchange field is inversely proportional to the AFM domain size. In the antidot arrays, the nanopores reduce the FM domain size more than in continuous films and also increase the random field, which is essential for an increased H_E.

As shown in Fig. 30, H_E and H_C decrease with increasing temperature because the thermal energy prevails over the exchange coupling between the AFM and FM layers. Interestingly, the blocking temperature (T_B, the temperature where the EB field completely disappears) of the antidot arrays is higher than that of the continuous films on Si and Al_2O_3, which indicates a larger effect of thermal activation in the continuous films. The blocking temperature varies with the pore diameter (d) and the higher T_B is observed in the antidot arrays compared with continuous films and the largest blocking temperature enhancement appears in the antidot arrays with $d = 40$ nm from the inset in Fig. 30. In comparison with the antidot arrays with smaller diameter of pores, the decrease of quantity of the pores and ratio of materials on the wall/top of AAO templates in the antidot arrays with $d = 128$ nm may reduce the contribution of the perpendicular magnetization component, causing the decrease of T_B. This effect of thermal activation is more pronounced in the continuous films than in the antidot arrays, which has rarely been reported.[91,107] The perpendicular magnetization component of the FM/AFM bilayers along the inner wall of the AAO is attributed to the enhanced in-plane T_B of the antidot arrays.

According to the random field model, the EB field H_E is related to the energy stored in the AFM domain wall

by $H_E \propto (A_{AF}K_{AF})^{1/2}$.[64] Assuming that A_{AF} is not dependent on temperature and that $K_{AF} = K_{AF}(0)(1 - T/T_N)^2$ for the cubic anisotropy of the AF layers, the model gives $H_E \propto \sqrt{A_{AF}K_{AF}(0)}(1 - T/T_N)$ for the temperature dependence of H_E. Substituting T_B for T_N results in $H_E \propto \sqrt{A_{AF}K_{AF}(0)}(1 - T/T_B)$. Taking into account both the out-of-plane K_1 and the in-plane anisotropy K_2, the NiO domain-wall energy can be expressed by[108] $\sigma_{AF}=2\sqrt{A_{AF}K_1}\cos\alpha + 2/3\sqrt{2A_{AF}K_2}\cos 6\beta$, where A_{AF} is the exchange stiffness, α the coherent angle out of the NiO (111) plane, β the coherent rotation angle from the easy axis $[\bar{1}2\bar{1}]$ within the NiO (111) plane. The temperature dependence of H_E can be expressed as $H_E \propto C^{(1)}(1 - T/T_B^{(1)})^{\gamma^{(1)}} + C^{(2)}(1 - T/T_B^{(2)})^{\gamma^{(2)}}$,[60] where $(T_B^{(1)}\gamma^{(1)})$ and $(T_B^{(2)}\gamma^{(2)})$ are determined by the temperature dependence of K_1 and K_2, respectively and $C^{(1)}$ and $C^{(2)}$ are constants. In the continuous films, the NiO domain-wall energy is dominated by the in-plane anisotropy constant K_2. The temperature dependence of H_E is mainly controlled by the temperature dependence of the in-plane anisotropy constant K_2. However, in antidot arrays, the out-of-plane anisotropy constant K_1 plays a more important role due to the misaligned magnetic moments at the edge and at the inner wall of the nanopores. The much larger K_1 leads to a higher blocking temperature T_B in the antidot arrays than in the continuous films. The higher blocking temperature in the antidot arrays, indicating an excellent thermal stability of these nanostructures, is attractive for spintronics applications.

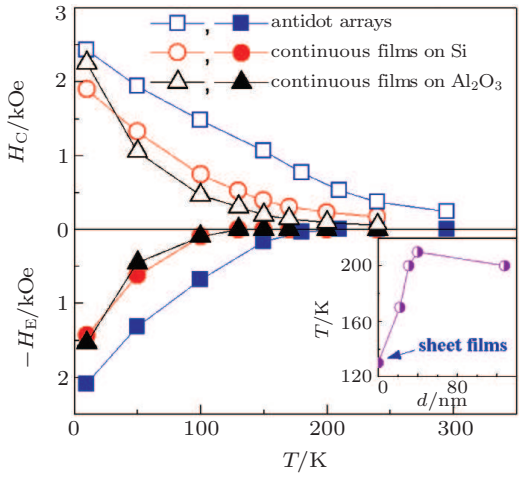


Fig. 30. Temperature dependence of H_E and H_C of Ag (10 nm)/Co (8 nm)/NiO (5 nm)/Ag (5 nm) antidot arrays with pore diameter of 40 nm (squares), and continuous films on Si and Al_2O_3 (circles and triangles). Inset: Temperature dependence of H_E for Ag (10 nm)/Co (8 nm)/NiO (5 nm)/Ag (5 nm) antidot arrays with pore diameters d and for continuous films on Si.[100]

In Co (3 nm)/NiO (6 nm)/Fe (10 nm) antidot arrays, the mean pore diameter and the center-to-center distance between the two adjacent pores are about 15 nm and 50 nm, respectively. Magnetic hysteresis loops (M–H) and magnetoresistance loops (R–H) at 10 K of the antidot arrays and continuous films have been recorded after FC at 2 kOe (Figs. 31(a)–31(d)). As can be seen in Figs. 31(a) and 31(b) (indicated by the dashed arrow), a magnetization step is found in the third quadrant for both samples. The gradual increase of the magnetization to its saturation value (M_S) obtained from the M–H loops at the saturation field (H_S), indicates a gradual orientation of the Co moments by the field (Fig. 31(a)), rather than a jump from step magnetization (M_P) to M_S in Fig. 31(b). The exchange-bias field H_E is 0.24 kOe and 0.4 kOe for the antidot arrays and the continuous films, respectively. Compared with the continuous films, the smaller H_E in antidot arrays is attributed to the three-dimensional effect modified by the nanopores.[100] As the film has misaligned FM and AFM moments at the edge and at wall of the nanopores, the interfacial AFM/FM coupling will be reduced, which leads to smaller H_E in the antidot arrays compared with continuous films. The magnetic moments at the interface between AFM and FM layers are neither parallel nor antiparallel but at an angle θ. The exchange-bias field can be expressed as $H_E \propto \sqrt{A_{AF}K_{AF}(0)}(1 - T/T_B)\cos\theta$.[64] Therefore, for constant thickness of FM and AFM layers, $J_E \propto (1 - T/T_B)\cos\theta$; $\theta = 0$ for the continuous film and $\theta \neq 0$ for the antidot arrays film. Because of the existence of an angle θ between AFM and FM and the surface roughness or defects of the film, the reversal of the Co moments will be gradual in Fig. 31(a) rather than the jump from M_P to M_S in Fig. 31(b), and also the gradual variation of R in Fig. 31(c). Positive MR is observed in Fig. 31(c), but negative MR in Fig. 31(d). The different M–H and R–H curves in Fig. 31 indicate that the change of microstructure induced by the AAO template strongly affects the magnetic and magnetotransport properties of Co/NiO/Fe trilayers. According to Jullière's expression, $\Delta R/R = (R_{AP}–R_P)/R_{AP} = 2P_1P_2/(1 + P_1P_2)$, where R_{AP} and R_P are the resistances in the antiparallel and parallel states, respectively and P_1 and P_2 the electron spin polarizations of the two magnetic electrodes.[70] The positive MR in Fig. 31(c) and negative MR in Fig. 10(d) indicate $R_{AP} > R_P$ in the nanostructured film but $R_{AP} < R_P$ in the continuous film. The current is parallel to the magnetic field direction and the easy axis of FM layers, which leads to anisotropic magnetoresistance in the continuous films after the FC procedure. However, the misaligned magnetic moments in the antidot arrays give rise to a magnetization component perpendicular to the current direction, which may lead to the difference in sign of magnetoresistance for the antidot arrays and the continuous films.[92,100] The antidot arrays change the sign of the electron spin polarization of one FM.

The temperature dependence of the magnetic properties of the trilayers obtained after ZFC is shown in Fig. 32. The M_S values for the antidot arrays are nearly constant from 10 K to 150 K and then decrease as temperature increases further,

while M_S values of the continuous film increase from 10 K to 100 K and then decrease again above 100 K. The nearly constant M_S of antidot arrays from 10 K to 150 K, as shown in Fig. 32, is due to the relatively weak interfacial coupling between AFM and FM at low temperatures.[72]

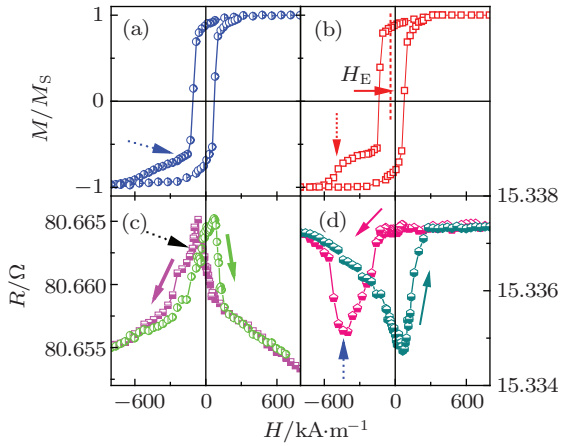


Fig. 31. Hysteresis loops M–H at 10 K after FC in 159.24 kA/m of (a) antidot arrays and (b) continuous films of Co (3 nm)/NiO (6 nm)/Fe (10 nm). The corresponding resistance loops R–H, recorded after FC in 159.24 kA/m, are shown in (c) and (d).[101]

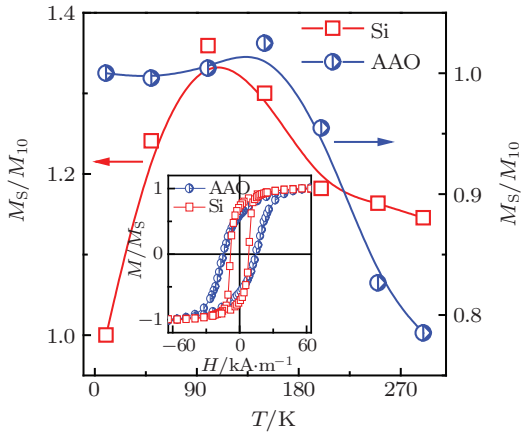


Fig. 32. Temperature dependence of the saturation magnetization M_S of antidot arrays and continuous films, recorded after ZFC. Inset: M–H loops at 290 K for antidot arrays and continuous films.[101]

The temperature dependence of the resistance (R–T) obtained after ZFC is shown in Figs. 33(a) and 33(b). Figures 33(c) and 33(d) exhibit $\mathrm{d}R/\mathrm{d}T$ versus T curves obtained from the data in Figs. 33(a) and 33(b). In Fig. 33(a), only one minimum R at 19 K is observed and R decreases linearly from 290 K to 47 K, and then increases non-linearly from 19 K to 2 K. However, in Fig. 33(b), R decreases linearly from 290 K to 193 K, and then rapidly increases to a maximum at 142 K. From 135 K to 47 K, R decreases linearly, followed by an exponential decrease at low temperatures. The different R–T curves for the two samples illustrate the influence of AAO template on transport properties of trilayers. In a magnetic-metal system, scattering processes occur at defects, by phonons or by spin-dependence electrons.[77] Competition between these processes may result in a low-temperature power law $R = R_0 + \alpha T^{\gamma}$.[77] The $R \propto T$ in Figs. 33(a) and 33(b) corresponds to metallic behavior. Because of the existence of surface roughness or defects in nanostructured films, R is greatly affected due to strong scattering, which results in an R value about ten times larger (81.56 Ω) for the antidot arrays than that (8.25 Ω) for the continuous films at 295 K. Moreover, the T_B at 193 K in Fig. 33(b) is the blocking temperature of NiO because of the disappearance of the exchange bias around T_B.[15] The disappearance of T_B at high temperatures in Fig. 33(a) may be due to strong spin scattering by the nanostructure. A minimum of R is observed at 19 K in Fig. 33(a), where the variation of R does not obey the power law $R = R_0 + \alpha T^{\gamma}$, associated with either localization or electron–electron interaction,[109] or with a Kondo effect.[110] The non-monotonous temperature dependence of R can be qualitatively understood in terms of the two-current model but not in terms of a Kondo mechanism.[78] The zero-field resistance R (T,0) can be expressed as

$$R(T,0) = R_F + R_N + R_S - \eta_N^2/R_N(\beta R_F + 2\gamma R_S)^2 - \eta_F^2/3R_F\beta^2, \quad (4)$$

where R_F, R_N and R_S are the resistance of FM, spacer layer and interface, respectively, η_F and η_N the order parameters of FM and spacer layer and β and γ the spin-asymmetry coefficients for FM layers and interface.[78] As the spin-diffusion length increases with decreasing temperature, the last term of the above equation (4) decreases with decreasing temperature, thus R (T,0) increases with decreasing temperature at low temperatures when R_F, R_N, and R_S are almost saturated. The effect in layered or granular magnetic systems is related to the spin-coupled interface resistance. The lower the temperature is, the weaker the spin relaxation and the higher the additional interface resistance.[111] Therefore, a minimum R at low temperatures is observed in the two samples.

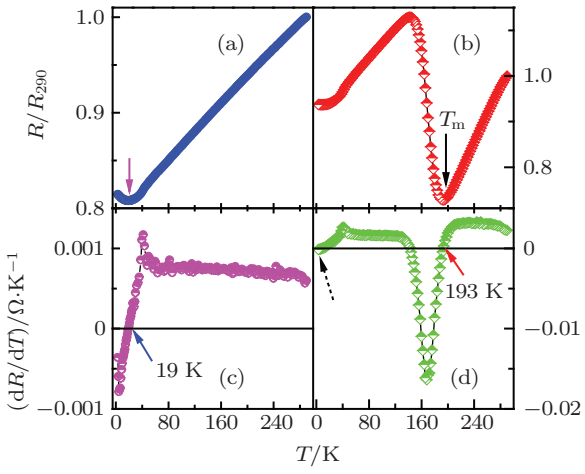


Fig. 33. Temperature dependence of the resistivity of (a) antidot arrays and (b) continuous films, recorded after ZFC. Figures 12(c) and 12(d) show the corresponding $\mathrm{d}R/\mathrm{d}T$ versus T curves.[101]

We have studied the EB effect in Co/NiO antidot arrays and continuous films. Compared with the continuous films, H_E of the antidot arrays can be enhanced or decreased by varying the thickness of the Co layer, which is due to the misalignment of the FM and AFM layers at the edge and at the inner wall of the nanopores. The antidot arrays have excellent thermal stability for application in spintronics devices. The obtained results explain the controversial reports in the literature[95,96,103] on the behavior of the EB field and its thermal stability in patterned nanostructures. Anomalous magnetic and magnetotransport properties are observed in both the Co/NiO/Fe antidot arrays and the continuous films. The observation of positive MR for the antidot arrays, but negative MR for the continuous films, is due to one FM layer's electron spin polarization being changed by the formation of the antidot arrays. Furthermore, the larger resistance and clear variation of resistance at low temperatures may be due to the stronger spin scattering and higher additional interface resistance in the nanostructure.

8. Conclusions

To provide a comprehensive understanding of exchange coupling, we have reviewed recent advances in the study of exchange couplings in several magnetic films, such as anisotropic hard/soft-magnetic multilayer films, FM/AFM/FM trilayers, [Pt/Co]/NiFe/NiO heterostructures, Co/NiO and Co/NiO/Fe trilayers on an anodic aluminum oxide (AAO) template. The conclusions are listed as follows:

In anisotropic hard/soft-magnetic multilayer films, a nonmagnetic spacer layer is inserted in between the textured hard- and soft-magnetic phase layers and the exchange-coupling interaction between the hard- and soft-magnetic phases is indirect and long-ranged. Thus, a new way is given to obtain a higher energy product in anisotropic nanocomposite hard/soft-magnetic multilayer films. In addition, when the magnetocrystalline anisotropy and thickness of the hard-magnetic phase layer decrease, the exchange-coupling interaction between the hard- and soft-magnetic phases is similar to the case of interlayer exchange coupling. When the nonmagnetic spacer layer is changed into an AFM layer, the interlayer and interfacial exchange couplings coexist in the system.

The competition between interlayer and interfacial exchange couplings is found to be temperature-dependent in Co (3 nm)/AF/Fe (10 nm) trilayers with AF $\equiv$ NiO, Cr_2O_3 or Cr. In the insulator case, the enhancement of the interlayer exchange coupling and the reduction of interfacial exchange coupling with increasing temperature results in a predominant interlayer exchange coupling at high temperature. In the metallic spacer case, both the couplings decrease with increasing temperature, resulting in decoupling at high temperatures. Furthermore, the competition between interfacial coupling between FM and AFM layers and interlayer coupling between two FM layers greatly affects the magnetotransport properties of trilayers. The sublayer greatly affects the magnetic anisotropy of bilayers and the interfacial coupling enhances the T_B of AFM materials.

Irreversible EB at the NiFe/NiO (FM/AFM) interface can be induced by FC, while reversible EB at the $[Pt/Co]_n$/NiFe (FM/FM) interface can be introduced by applying a saturation field. The reversible EB allows us to obtain different EB values isothermally. Such control of EB in these heterostructures is attractive for spintronics applications.

Compared with the sheet films, the H_E of the antidot arrays can be enhanced or decreased by varying the thickness of the Co layer, which is due to the misalignment of the FM and AFM layers at the edge and at the inner wall of the nanopores. The AAO template affects the interfacial exchange coupling between AFM and FM layers. The antidot arrays have excellent thermal stability for application in spintronics devices.

In a word, the results mentioned above may be favorable for understanding the interlayer between FM layers and interfacial exchange couplings in the interface of FM/AFM layer in the spin valve, which is helpful to design spintronics devices.

References

[1] Coehoorn R, de Mooij D B and de Waard C 1989 *J. Magn. Magn. Mater.* **80** 101
[2] Kneller E F and Hawig R 1991 *IEEE Trans. Magn.* **27** 3588
[3] Skomski R and Coey J M D 1993 *Phys. Rev.* B **48** 15812
[4] Al-Omari A and Sellmyer D J 1995 *Phys. Rev.* B **52** 3441
[5] Liu J P, Liu Y, Skomski R and Sellmyer D J 1999 *IEEE Trans. Magn.* **35** 3241
[6] Shindo M, Ishizone M, Sakuma A, Kato H and Miyazaki T 1997 *J. Appl. Phys.* **81** 4444
[7] Liu W, Zhang Z D, Liu J P, Chen L J, He L L, Liu Y, Sun X K and Sellmyer D J 2002 *Adv. Mater.* **14** 1832
[8] Ao Q, Zhang W L and Wu J S 2006 *J. Magn. Magn. Mater.* **299** 440
[9] Zhang J, Takahashi Y K, Gopalan R and Hono K 2005 *Appl. Phys. Lett.* **86**122509
[10] Grünberg P, Schreiber R, Pang Y, Brodsky M B and Sowers H 1986 *Phys. Rev. Lett.* **57** 2442
[11] Cui W B, Zheng S J, Liu W, Ma X L, Yang F, Yao Q, Zhao X G and Zhang Z D 2008 *J. Appl. Phys.* **104** 053903
[12] Grünberg P, Schreiber R, Pang Y, Brodsky M B and Sowers H 1986 *Phys. Rev. Lett.* **57** 2442
[13] Baibich M N, Broto J M, Fert A, Nguyen Van Dau F, Petroff F, Etienne P, Creuzet G, Friederich A and Chazelas J 1988 *Phys. Rev. Lett.* **61** 2472
[14] Cui W B, Liu W, Yang F, Lü X K, Liu X H, Guo S, Gong W J and Zhang Z D 2011 *J. Appl. Phys.* **109** 07A717
[15] Cui W B, Liu W, Li J, Yang F, Zhang Q, Liu X G and Zhang Z D 2008 *J. Appl. Phys.* D **41** 245007
[16] Cui W B, Liu W, Gong W J, Liu X H, Guo S, Yang F, Wang Z H and Zhang Z D 2012 *J. Appl. Phys.* **111** 07B503
[17] Kronmüller H, Durst K D and Sagawa M 1988 *J. Magn. Magn. Mater.* **74** 291
[18] Kou X C and Kronmüller H 1994 *J. Phys: Condens. Matter* **6** 6691
[19] Zhang H W, Sun Z G, Zhang S Y, Han B S and Shen B G 1999 *Phys. Rev.* B **60** 64
[20] Kronmüller H, Durst K D and Martinek G 1987 *J. Magn. Magn. Mater.* **69** 149
[21] Parkin S S P 1991 *Phys. Rev. Lett.* **66** 2152
[22] Gökemeijer N J, Ambrose T and Chien C L 1997 *Phys. Rev. Lett.* **79** 4270
[23] Hankel O 1964 *Phys. Stat. Solidi* **7** 919

[24] Parkin S S P, More N and Roche K P 1990 *Phys. Rev. Lett.* **64** 2304
[25] Parkin S S P 1991 *Phys. Rev. Lett.* **67** 3598
[26] Inomata K and Saito Y 1992 *Appl. Phys. Lett.* **61** 726
[27] Saito Y, Hashimoto S and Inomata K 1992 *Appl. Phys. Lett.* **60** 2436
[28] Parkin S S P 1992 *Appl. Phys. Lett.* **60** 512
[29] Parkin S S P, Li Z G and Smith D J 1991 *Appl. Phys. Lett.* **58** 2710
[30] Fawcett E 1988 *Rev. Mod. Phys.* **60** 209
[31] Unguris J, Celotta R J and Pierce D T 1991 *Phys. Rev. Lett.* **67** 140
[32] Unguris J, Celotta R J and Pierce D T 1992 *Phys. Rev. Lett.* **69** 1125
[33] Brumo P and Chappert C 1991 *Phys. Rev. Lett.* **67** 1602
[34] Lathiotakis N N, Györffy B L, Bruno E and Ginatempo B 2000 *Phys. Rev.* B **62** 9005
[35] Okuno S N and Inomata K 1993 *Phys. Rev. Lett.* **70** 1711
[36] Fretwell H M, Dugdale S B, Alam M A, Hedley D C R, Gonzalez A R and Palmer S B 1999 *Phys. Rev. Lett.* **82** 3867
[37] Bruno P 1993 *Europhys. Lett.* **28** 615
[38] Johnson M T, van de Vorst M T H, Bloemen P J H, Coehoom R, Reinders A, aan de Stegge J and Jungblut 1995 *Phys. Rev. Lett.* **75** 4686
[39] Coehoom R and Duchateau J P W B 1993 *J. Magn. Magn. Mater.* **126** 390
[40] Kubota H, Ishio S and Miyazaki T 1993 *J. Magn. Magn. Mater.* **126** 463
[41] Filipkowski M E, Krebs J J, Prinz G A and Gutierrez C J 1995 *Phys. Rev. Lett.* **75** 1847
[42] van der Heijden P A A, Swuste C H, De Jonge W J M, Gaines J M, Van Eemeren J T W M and Schep K M 1999 *Phys. Rev. Lett.* **82** 1020
[43] Yang F Y and Chien C L 2000 *Phys. Rev. Lett.* **85** 2597
[44] Camarero J, Pennec Y, Vogel J, Bonfim M, Pizzini S, Ernult F, Fettar F, Garcia F, Lancon F, Billard L, Dieny B, Tagliaferri A and Brookes N B 2003 *Phys. Rev. Lett.* **91** 027201
[45] Yafet Y 1987 *Phys. Rev.* B **36** 3948
[46] Bruno P and Chappert C 1991 *Phys. Rev. Lett.* **67** 1602
[47] Erickson R P, Hathaway K B and Cullen J R 1993 *Phys. Rev.* B **47** 2626
[48] Slonczewski J C 1993 *J. Magn. Magn. Mater.* **126** 374
[49] Edwards D M, Mathon J, Muniz R B and Phan M S 1991 *Phys. Rev. Lett.* **67** 493
[50] Wang Y, Levy P M and Fry J L 1990 *Phys. Rev. Lett.* **65** 2732
[51] Shi Z P, Levy P M and Fry J L 1992 *Phys. Rev. Lett.* **69** 3678
[52] Bruno P 1992 *J. Magn. Magn. Mater.* **116** L13
[53] Costa A T Jr, d'Albuquerque e Castro J D and Muniz R B 1997 *Phys. Rev.* B **56** 13697
[54] Ortega J E and Himpsel F J 1992 *Phys. Rev. Lett.* **69** 844
[55] Bruno P 1995 *Phys. Rev.* B **52** 411
[56] Stiles M D 1993 *Phys. Rev.* B **48** 7238
[57] Bruno P 1993 *J. Magn. Magn. Mater.* **121** 248
[58] Liu X H, Liu W, Yang F, Lü X K, Cui W B, Guo S, Gong W J and Zhang Z D 2009 *Appl. Phys. Lett.* **95** 222505
[59] Nogués J, Sort J, Langlais V, Skumryev V, Suriñach S, Muñoz J S and Baró M D 2005 *Phys. Rep.* **422** 65
[60] Liu Z Y and Adenwalla S 2003 *Phys. Rev. Lett.* **91** 037207
[61] Wohlfarth E P 1980 *Ferromagnetic Materials* (Amslerdam: North-Holland Press)
[62] Barnier Y, Pauthenet R and Rimet G 1961 *Acad. Sci. Paris, C. R.* **252** 2839
[63] Lindner J, Rüdt C, Kosubek E, Poulopoulos P, Baberschke K, Blomquist P, Wäppling R and Mills D L 2002 *Phys. Rev. Lett.* **88** 167206
[64] Malozemoff A P 1987 *Phys. Rev.* B **35** 3679
[65] Blamire M G, Ali M, Leung C W, Marrows C H and Hickey B J 2007 *Phys. Rev. Lett.* **98** 217202
[66] Mills D. L 1968 *Phys. Rev. Lett.* **20**18
[67] Lines M E 1963 *Phys. Rev.* **131** 546
[68] Liu X H, Liu W, Guo S, Yang F, Lü X K, Gong W J and Zhang Z D 2010 *Appl. Phys. Lett.* **96** 082501
[69] Liu X H, Liu W, Guo S, Lü X K, Gong W J and Zhang Z D 2011 *J. Alloys Compd.* **509** 1448
[70] De Teresa J M, Barthelemy A, Fert A, Contour J P, Montaigne F and Seneor P 1999 *Science* **286** 507
[71] Rusanov A Y, Habraken S and Aarts J 2006 *Phys. Rev.* B **73** 060505
[72] Liu X H, Liu W, Guo S, Gong W J, Feng J N and Zhang Z D 2010 *Appl. Phys. Lett.* **97** 072502
[73] Liu X H, Cui W B, Lü X K, Liu W, Zhang X G, Li D and Zhang Z D 2008 *J. Appl. Phys.* **103** 103906
[74] Park M H, Hong Y K, Gee S H, Mottern M L, Jang T W and Burkett S 2002 *J. Appl. Phys.* **91** 7218
[75] Meiklejohn W H 1958 *J. Appl. Phys.* **29** 454
[76] Liu X H, Liu W, Lü X K, Yang F, Wei X, Zhang Z D and Sellmyer D J 2010 *J. Appl. Phys.* **107** 083919
[77] Verschoren G, Dobrynin A N, Temst K, Silverans R E, Van Haesendonck C, Lievens P, Pipeleers B, Zhou S Q, Vantomme A and Bras W 2008 *Thin Solid Films* **516** 8232
[78] Gerber A, Milner A, Korenblit I Y, Karpovsky M, Gladkikh A and Sulpice A 1998 *Phys. Rev.* B **57** 13667
[79] Maat S, Takano K, Parkin S S P and Fullerton E E 2001 *Phys. Rev. Lett.* **87** 087202
[80] Nogués J, Stepanow S, Bollero A, Sort J, Dieny B, Nolting F and Gambardella P 2009 *Appl. Phys. Lett.* **95** 152515
[81] Sort J, Popa A, Rodmacq B and Dieny B 2004 *Phys. Rev.* B **70** 174431
[82] Cain W C and Kryder M H 1990 *J. Appl. Phys.* **67** 5722
[83] Nogués J, Sort J, Suriñach S, Muñoz J S, Baro M D, Bobo J F, Lüders U, Haanappel E, Fitzsimmons M R, Hoffmann A and Cai J W 2003 *Appl. Phys. Lett.* **82** 3044
[84] Yang P Y, Zhu X Y, Zeng F and Pan F 2009 *Appl. Phys. Lett.* **95** 172512
[85] Gong W J, Liu W, Liu X H, Guo S, Feng J N, Li Bo and Zhang Z D 2011 *J. Appl. Phys.* **109** 043906
[86] Huang P H, Huang H H and Lai C H 2007 *Appl. Phys. Lett.* **90** 062509
[87] Bollero A, Buda-Prejbeanu L D, Baltz V, Sort J, Rodmacq B and Dieny B 2006 *Phys. Rev.* B **73** 144407
[88] van der Zaag P J, Ijiri Y, Borchers J A, Feiner L F, Wolf R M, Gaines J M, Erwin R W and Verheijen M A 2000 *Phys. Rev. Lett.* **84** 6102
[89] Ohldag H, Scholl A, Nolting F, Arenholz E, Maat S, Young A T, Carey M and Stohr J 2003 *Phys. Rev. Lett.* **91** 017203
[90] Liu K, Baker S M, Tuominen M, Russell T P and Schuller I K 2001 *Phys. Rev.* B **63** 060403
[91] Adeyeye A O and Tripathy D 2009 *Phys. Rev.* B **79** 064413
[92] Adeyeye A O, Bland J A C and Daboo C 1997 *Appl. Phys. Lett.* **70** 3164
[93] Chuang V P, Jung W, Ross C A, Cheng J Y, Park O H and Kim H C 2008 *J. Appl. Phys.* **103** 074307
[94] Schulze C, Faustini M, Lee J, Schletter H, Lutz M U, Krone P, Gass M, Sader K, Bleloch A L, Hietschold M, Fuger M, Suess D, Fidler J, Wolff U, Neu V, Grosso D, Makarov D and Albrecht M 2010 *Nanotechnology* **21** 495701
[95] Tripathy D, Adeyeye A O andSingh N 2008 *Appl. Phys. Lett.* **93** 022502
[96] Rahman M T, Shams N N, Wang D S and Lai C H 2009 *Appl. Phys. Lett.* **94** 082503
[97] Wang C C, Adeyeye A O, Singh N, Huang Y S and Wu Y H 2005 *Phys. Rev.* B **72** 174426
[98] Rahman M T, Shams N N, Lai C H, Fidler J and Suess D 2010 *Phys. Rev.* B **81** 014418
[99] Rahman M T, Shams N N, Wang D S and Lai C H 2009 *Appl. Phys. Lett.* **94** 082503
[100] Gong W J, Yu W J, Liu W, Guo S, Ma S, Feng J N, Li B and Zhang Z D 2012 *Appl. Phys. Lett.* **101** 012407
[101] Liu X H, Gong W J, Liu W, Guo S, Feng J N and Zhang Z D 2012 *Thin Solid Films* **526** 278
[102] Li A P, Muller F, Birner A, Nielsch K and Gosele U 1998 *J. Appl. Phys.* **84** 6023
[103] Fettar F, Cagnon L and Rougemaille N 2010 *Appl. Phys. Lett.* **97** 192502
[104] O'Grady K, Fernandez-Outon L E and Vallejo-Fernandez G 2010 *J. Magn. Magn. Mater.* **322** 883
[105] Suess D, Fidler J, Porath K, Schrefl T and Weller D 2006 *J. Appl. Phys.* **99** 08G905
[106] Matsuyama H, Haginoya C and Koike K 2000 *Phys. Rev. Lett.* **85** 646
[107] Baltz V, Sort J, Rodmacq B, Dieny B and Landis S 2005 *Phys. Rev.* B **72** 104419
[108] Matsuyama H, Haginoya C and Koike K 2000 *Phys. Rev. Lett.* **85** 646
[109] Aliev F G, Kunnen E, Temst K, Mae K, Verbanck G, Barnas J, Moshchalkov V V and Bruynseraede Y 1997 *Phys. Rev. Lett.* **78** 137
[110] Gruner G and Zawadowski A 1974 *Rep. Prog. Phys.* **37** 1497
[111] van Son P C, van Kempen H and Wyder P 1987 *Phys. Rev. Lett.* **58** 2271